

1 Self-similar slip pulses during rate-and-state
2 earthquake nucleation

Allan M. Rubin

3 Department of Geosciences, Princeton University, Princeton, New Jersey,
4 USA

Jean-Paul Ampuero

5 Seismological Laboratory, Caltech, Pasadena, California, USA

A. M. Rubin, Department of Geosciences, Princeton University, Princeton, NJ 08544, (email: arubin@princeton.edu)

6 **Abstract.** For a wide range of conditions, earthquake nucleation zones
7 on rate- and state-dependent faults that obey either of the popular state evo-
8 lution laws expand as they accelerate. Under the “slip” evolution law, which
9 experiments show to be the more relevant law for nucleation, this expansion
10 takes the form of a unidirectional slip pulse. In numerical simulations these
11 pulses often tend to approach, with varying degrees of robustness, one of a
12 few styles of self-similar behavior. Here we obtain an approximate self-similar
13 solution that accurately describes slip pulses growing into regions initially
14 sliding at steady state. In this solution the length scale over which slip speeds
15 are significant continually decreases, being inversely proportional to the log-
16 arithm of the maximum slip speed V_{max} , while the total slip remains con-
17 stant. This slip is close to $D_c(1-a/b)^{-1}$, where D_c is the characteristic slip
18 scale for state evolution and a and b are the parameters that determine the
19 sensitivity of the frictional strength to changes in slip rate and state. The
20 pulse has a “distance to instability” as well as a “time to instability”, with
21 the remaining propagation distance being proportional to $(1-a/b)^{-2}[\ln(V_{max}\theta_{bg}/D_c)]^{-1}$,
22 where θ_{bg} is the background state into which the pulse propagates. This so-
23 lution provides a reasonable estimate of the total slip for pulses growing into
24 regions that depart modestly from steady state.

1. Introduction

25 One motivation for developing constitutive laws for fault slip has been to model quasi-
26 static earthquake nucleation. An early goal of such models was to assess the feasibility of
27 detecting the nucleation phase of large earthquakes, hopefully with enough lead time to be
28 useful for hazards mitigation [*Dieterich and Kilgore, 1996*]. It is also conceivable that the
29 nucleation process sets the stage for the earliest portions of dynamic rupture [*Ellsworth
30 and Beroza, 1995*], seismic signals from which might be used for earthquake early warning
31 systems [*Olson and Allen, 2005*]. More recently, the same models that have been applied
32 to nucleation have been used to study episodic slow slip in subduction zones [*Kato, 2003*;
33 *Shibazaki and Iio, 2003*; *Liu and Rice, 2005*; *Rubin, 2008*]. In addition, a professed goal
34 of ongoing experiments along the San Andreas fault and in deep South African mines
35 is to detect the nucleation of small earthquakes at seismogenic depths [*Ellsworth et al.,
36 2007*; *Reches et al., 2004*]. Interpreting such observations is likely to require a greater
37 understanding of nucleation than we currently possess.

38 Impediments to using numerical models to increase our understanding of earthquake
39 nucleation come from at least 3 sources: (1) Uncertainty regarding the appropriate con-
40 stitutive law for friction, (2) uncertainty regarding the relevant initial and boundary con-
41 ditions along the fault, and (3) the difficulty in discerning how the friction law interacts
42 with elasticity to define the characteristics of the nucleation zone. Uncertainty regard-
43 ing the appropriate values of the frictional parameters is also an issue, but this probably
44 pales in comparison to (1). It is the nonlinearity of the governing equations that makes
45 (2) and (3) such significant hurdles. The complexity of elastic/frictional systems, and

46 their sensitivity to both material properties and loading conditions, can make it difficult
47 to extrapolate beyond the results of numerical simulations already carried out.

48 For modeling quasi-static fault slip, rate- and state-dependent friction is thought to be a
49 good compromise between simplicity and completeness [*Dieterich*, 1979; *Ruina*, 1983; *Rice*
50 *et al.*, 2001]. *Rubin and Ampuero* [2005] obtained analytical estimates of the length and
51 time scales of nucleation (addressing item 3 above) for the particular case of faults obeying
52 the “aging” law for state evolution. For laboratory values of the rate-and-state parameters
53 a and b and a seemingly wide range of initial and boundary conditions (e.g., relatively
54 homogeneous faults under steady loading), such nucleation zones grow as quasi-statically
55 expanding cracks and can approach a well-defined limiting size. This size is much larger
56 than both that observed numerically by *Dieterich* [1992], and that anticipated on the basis
57 of critical stiffness arguments [*Rice et al.*, 2001]. Subsequent work has shown that this
58 nucleation length arises also in radiation damping or fully elastodynamic earthquake cycle
59 simulations that include adjoining velocity-weakening and velocity-strengthening regions
60 (e.g. figures 6 of *Rubin* [2008] and *Chen and Lapusta* [2009], noting in the latter case that
61 the length scale in 3-D is larger than in 2-D by the factor $\pi^2/4$).

62 This crack-like expansion and large size result from the large increase in fracture energy
63 with increasing slip speed implied by the aging law. This large increase in fracture energy
64 in turn comes from the increase in the effective slip-weakening distance with the logarithm
65 of the velocity jump at the margins of the expanding nucleation zone. However, as was
66 noted in retrospect by *Rubin and Ampuero* [2005], there is no experimental evidence for
67 this increase in slip-weakening distance. Experiments show instead that the slip-weakening
68 distance seems to be independent of the magnitude of the velocity jump [*Nakatani*, 2001],

69 a property that is well-modeled by the “slip” evolution law [*Ruina*, 1983; *Bayart et al.*,
70 2006].

71 *Ampuero and Rubin* [2008] found that for the slip law, nucleation zones expand not
72 as cracks but as unidirectional slip pulses. Although they noted that their simulations
73 appeared nearly self-similar in many respects, they were unable to obtain analytical de-
74 scriptions comparable to those for the aging law. In this paper we derive an approximate
75 self-similar solution for a particular class, and arguably the most basic class, of these slip
76 pulses. By self-similar we mean that given a solution for any particular quantity (e.g.,
77 slip) as a function of position at one time, one can determine that same quantity at any
78 later time simply by a suitable rescaling of the relevant coordinate axes. Such solutions,
79 and even the scaling relations alone, can be very useful for interpreting the results of com-
80 plex numerical simulations and extrapolating beyond those already carried out. Scaling
81 of the position axis is done here in the reference frame of the moving pulse tip. Deter-
82 mining the time-dependence of the solution explicitly requires solving a transcendental
83 equation for the maximum slip speed; however, that time dependence can be expressed
84 much more simply in terms of the maximum slip speed itself, so we emphasize that view
85 here. Some pulse attributes, such as the scaling of the total slip and stress drop with a/b ,
86 can be deduced from a general consideration of the observed self-similarity alone; this is
87 the subject of Section 4. Section 5 outlines the particular self-similar solution, which is
88 needed to estimate the detailed spatial variation of slip and the rate of acceleration to
89 instability. We also compare the scaling of nucleation under the slip and aging laws, and,
90 in light of items (1) and (2) enumerated above, consider when the pulses described here
91 might be relevant to natural faults.

2. Background

92 We adopt a standard equation for the frictional strength τ ,

$$93 \quad \tau = \sigma \left[f^* + a \ln \frac{V}{V^*} + b \ln \frac{V^* \theta}{D_c} \right] \quad (1)$$

94 [e.g. *Marone, 1998*], where σ is the effective normal stress, V is the sliding velocity, θ is
 95 the variable with units of time describing the fault state, D_c is the characteristic sliding
 96 distance for the evolution of θ , and a and b determine the response to changes in sliding
 97 velocity and state (for a listing of frequently-cited parameters see Table 1). f^* and V^*
 98 are reference values of the friction and velocity and exert no influence on the system.
 99 Characteristic laboratory values of D_c are 1–100 μm , while a and b are typically of order
 100 10^{-2} . When $a < b$ the fault is steady-state velocity weakening and instability is possible;
 101 we assume this to be the case here. Laboratory values of a/b are very often > 0.9 , i.e.
 102 close to velocity-neutral, even for velocity-weakening faults [*Kilgore et al., 1993; Blanpied*
 103 *et al., 1998*].

104 For quasi-static deformations we equate the frictional strength from (1) with the fault
 105 stress, which we partition into a boundary condition $\tau^\infty(x, t)$ and an elastic component
 106 $\tau^{el}(x, t)$ due to nonuniform fault slip. In two dimensions the static elastic stresses due to
 107 nonuniform slip are

$$108 \quad \tau^{el}(x) = \frac{\mu'}{2\pi} \int_{-\infty}^{\infty} \frac{d\delta/ds}{s-x} ds, \quad (2)$$

109 where δ is slip and μ' is the elastic shear modulus for anti-plane deformation or the shear
 110 modulus divided by one minus Poisson's ratio for plane strain deformation.

111 To close the system of equations we need an evolution law for the state variable. Two
 112 have been commonly used, both largely empirical:

$$113 \quad \dot{\theta} = 1 - \frac{V\theta}{D_c} \quad (\text{Aging law}) ; \quad (3)$$

$$114 \quad \dot{\theta} = -\frac{V\theta}{D_c} \ln \frac{V\theta}{D_c} \quad (\text{Slip law}) . \quad (4)$$

116 Both laws exhibit steady-state behavior ($\dot{\theta} = 0$) when $V\theta/D_c = 1$, and for $V\theta/D_c \sim 1$
 117 they are asymptotically identical. When $V\theta/D_c \ll 1$, $\dot{\theta} \sim 1$ for the aging law (time-
 118 dependent strengthening) but $\dot{\theta} \ll 1$ for the slip law (no evolution in the absence of
 119 slip). The former behavior is more consistent with the observed strengthening during the
 120 “hold” portions of slide-hold-slide experiments, when slip speeds are extremely low and
 121 $V\theta/D_c \ll 1$ [*Dieterich and Kilgore, 1994; Beeler et al., 1994*]. However, it is the behavior
 122 of the fault from $V\theta/D_c \sim 1$ to $V\theta/D_c \gg 1$ that determines the nucleation style [*Rubin*
 123 *and Ampuero, 2005; Ampuero and Rubin, 2008; Rubin, 2008, Figure A1*]. The pertinent
 124 difference between the laws for $V\theta/D_c \gg 1$ is that the effective slip-weakening distance for
 125 the return to steady state increases as $\log(V\theta/D_c)$ for the aging law, but is independent
 126 of $V\theta/D_c$ for the slip law. Laboratory experiments are much more consistent with the
 127 slip law in this regard, and in fact that law appears to work quite well when $V\theta/D_c \gg 1$
 128 [*Ruina, 1983; Bayart et al., 2006*], at least at slip speeds up to hundreds of microns per
 129 second. This is the motivation for obtaining an analytic description of nucleation under
 130 the slip law.

131 As discussed by *Rubin and Ampuero [2005]* and *Ampuero and Rubin [2008]*, the velocity
 132 jump at the margin of an expanding nucleation zone is close enough to instantaneous that
 133 it can be treated as such when estimating the stress evolution behind the front. With this

134 approximation, the fracture energy G_c for the slip law is

$$135 \quad G_c = b\sigma D_c \ln \frac{V_{max}\theta_{bg}}{D_c} , \quad (5)$$

136 where V_{max} is the maximum slip speed behind the nucleation front and θ_{bg} is the back-
 137 ground value of state (not necessarily at steady state) ahead of the front. As the
 138 $b \ln(V^*\theta/D_c)$ term in (1) is sometimes written as Ψ [e.g., *Perrin et al.*, 1995], for shorthand
 139 we write (with no b)

$$140 \quad \Psi_0(t) = \ln \frac{V_{max}(t)\theta_{bg}}{D_c} . \quad (6)$$

141 In all our simulations, for both the aging and slip laws the slip speed ahead of the front is
 142 low enough that there is very little state evolution until the pulse tip (peak stress) arrives.
 143 Thus θ_{bg} is well defined. This is analogous to slide-hold-slide laboratory experiments in
 144 which the true sliding velocity upon reloading following a “hold” does not instantaneously
 145 track the load-point velocity, but reaches that velocity with minimal evolution of θ . Ne-
 146 glecting this evolution introduces errors that seem comparable to those associated with
 147 the standard “small-scale-yielding” assumption of linear elastic fracture mechanics.

148 For a crack tip propagating at quasi-static equilibrium, the energy for fracture is pro-
 149 vided by the mechanical energy release rate G . When using superposition it is more
 150 convenient to work with stress intensity factors K , which add linearly. In that case the
 151 equilibrium condition equivalent to $G = G_c$ is $K = K_c$, where the fracture toughness K_c
 152 is related to G_c via $K_c^2 = 2\mu'G_c$ [*Lawn*, 1993]. Thus from (5),

$$153 \quad K_c = (2\mu'b\sigma D_c \Psi_0)^{1/2} . \quad (7)$$

3. Numerical slip pulses

Figure 1 shows snapshots of 2 styles of slip pulses observed by *Ampuero and Rubin* [2008]. Initial conditions are shown in red. In both examples the fault started below steady state ($V\theta/D_c < 1$) except for a localized asymmetric perturbation that reached steady state at $x = 0$. A small background loading rate was applied. The initial perturbation decayed more slowly to the left, such that a pulse initiated on the left and reached large slip speeds before a pulse developed on the right. Distances in Figure 1 are normalized by L_b , defined as

$$L_b = \frac{\mu' D_c}{b\sigma} . \quad (8)$$

L_b is the relevant length scale under the aging law when $V\theta/D_c \gg 1$ [*Dieterich, 1992; Rubin and Ampuero, 2005*]; the corresponding length scale for the slip law is $L_b/\ln(V\theta/D_c)$, where V and θ are representative local values [*Ampuero and Rubin, 2008*].

Note that the snapshots in Figure 1 are plotted at equal increments of $\log(V_{max})$ and not time; the time intervals become dramatically shorter (very roughly as D_c/V_{max}) as the pulse accelerates to instability. Because there is a unique relation, fixed by the evolution law, between the maximum slip speed and the pulse propagation speed [*Ampuero and Rubin, 2008*, and equation (31) to follow], the two pulses in Figure 1 have essentially the same propagation speed when compared at the same V_{max} . Thus nucleation in Figure 1a is accelerating to instability more rapidly than in Figure 1f, in that the pulse propagates a shorter distance, at the same propagation speed, between neighboring values of V_{max} .

We refer to the length scale behind the tip over which significant slip is accumulating as the pulse width; reasonable values are $\sim 2L_b$ and $10L_b$ for the final snapshots in Figures 1b and 1g, respectively. For the pulse on the left the total slip remains approximately constant

176 as the pulse width varies as Ψ_0^{-1} . Figure 2b shows that when distances are stretched by
 177 Ψ_0 the displacement profiles appear to asymptotically approach a fixed distribution; this
 178 suggests that a self-similar solution might be found. For the pulse on the right, both
 179 the peak slip and the pulse width increase in proportion to Ψ_0 , so when both axes are
 180 reduced by this quantity the displacement profiles again asymptotically approach a fixed
 181 distribution (Figure B1b). *Ampuero and Rubin* [2008, figure 7] also observed a third style
 182 of pulse in which the pulse width varied relatively little while the peak slip increased
 183 roughly as $\Psi_0^{1/2}$ (Figure B1e).

184 For any given V_{max} the fracture energy is $b\sigma D_c \Psi_0$, independent of the pulse style. For
 185 a stress distribution $\Delta\tau$ acting over a distance L behind the tip of a semi-infinite crack,
 186 the mechanical energy release rate G , that must balance G_c , is dimensionally

$$187 \quad G \sim \frac{L\Delta\tau^2}{\mu'} \quad (9)$$

188 [*Lawn*, 1993], while from elasticity

$$189 \quad \Delta\tau \sim \mu' \frac{\delta}{L}. \quad (10)$$

190 If we assume

$$191 \quad \delta/D_c \propto \Psi_0^p, \quad (11)$$

192 where p is some growth exponent, then with $G = G_c \propto \Psi_0$ (equations 5 and 6), equations
 193 (9)–(10) imply

$$194 \quad \Delta\tau/b\sigma \propto \Psi_0^{(1-p)}; \quad (12)$$

$$195 \quad L/L_b \propto \Psi_0^{(2p-1)}. \quad (13)$$

197 The pulses we have observed numerically correspond to $p = 0$ (left column of Figure 1),
 198 $p = 1$ (right column), and $p = 1/2$ (right column of Figure B1). For example, in Figures
 199 1c and 2c the maximum stress drop, reached just behind the tip, is proportional to Ψ_0 ,
 200 consistent with $p = 0$ (equation 12).

201 *Ampuero and Rubin* [2008] also noted that each style of pulse was associated with its
 202 own rate of acceleration to instability. Empirically their results are consistent with

$$203 \quad \frac{\dot{V}_{max} D_c}{V_{max}^2} \propto \Psi_0^{-2p+1}, \quad (14)$$

204 where $\dot{V}_{max} \equiv dV_{max}/dt$. In Appendix B we will show that (14) follows from the observed
 205 self-similarity of the velocity profiles. For $p = 1/2$ (14) becomes $\dot{V}_{max} D_c / V_{max}^2 = \text{const.}$,
 206 the same as for all nucleation regimes under the aging law [*Dieterich, 1992; Rubin and*
 207 *Ampuero, 2005*]. In this case the time remaining to instability varies as D_c / V_{max} . The
 208 larger value of the exponent in (14) for $p = 0$ than for $p = 1$ seems consistent with the
 209 more rapid approach to instability in Figure 1a than in Figure 1f, although buried in the
 210 implied proportionality constant is an unspecified dependence upon a/b and p that could
 211 also influence this.

212 Coupled with the observation that $V\theta/D_c$ approaches steady state near the stress min-
 213 imum behind the pulse tip (Figures 1e and 1j, see also Figure 7 of *Ampuero and Rubin*
 214 [2008]), equation (12) implies that the pulse style is closely tied to the ambient conditions
 215 along the fault. To see this, we can write $\Delta\tau_{min} = \tau_{bg} - \tau_{min}$, where τ_{bg} is the background
 216 stress and τ_{min} the stress minimum. Manipulating (1) with the constraint of being at

217 steady state at τ_{min} with slip speed $\sim V_{max}$ leads to

$$218 \quad \frac{\Delta\tau_{min}}{b\sigma} = \left(\frac{a}{b} - 1\right) \Psi_0 - \frac{a}{b} \Psi_{bg} , \quad (15)$$

219 where $\Psi_{bg} \equiv \ln(V_{bg}\theta_{bg}/D_c)$. Thus $\Delta\tau_{min}$ will be proportional to Ψ_0 ($p = 0$; left column
 220 of Figure 1) if the pulse propagates into a region initially at steady state ($\Psi_{bg} = 0$). For
 221 $\Delta\tau_{min}$ to be constant, on the other hand ($p = 1$; right column of Figure 1), equation
 222 (15) requires an a/b -dependent linear relation between $\Psi_{bg}(t)$ and $\Psi_0(t)$. Graphically, the
 223 ambient stress must decrease in the direction of pulse propagation in parallel with the
 224 steady-state strength, as can be seen in Figure 1h. Such considerations provide insight
 225 into how the different initial conditions in Figure 1 gave rise to the different pulse styles
 226 observed. For the example on the left, the pulse propagated into a region outside the initial
 227 perturbation where Ψ_{bg} was quasi-constant and close to steady state. For the example
 228 on the right, the pulse propagated within the initial perturbation, in a region where Ψ_{bg}
 229 decreased quasi-linearly in the propagation direction.

230 All 3 pulse styles exhibit the same scaling within the region of large strength loss
 231 immediately behind the pulse front [*Ampuero and Rubin, 2008, Figure 10e*]. The reason
 232 is that this strength loss is dominated by state evolution under conditions of near-constant
 233 slip speed, and this is a universal property of the evolution law. We refer to this as the
 234 near-tip or slip-weakening region. Its length R is given dimensionally by

$$235 \quad R \sim \delta_c \frac{\mu'}{\Delta\tau_{p-r}} = \delta_c \frac{\mu'}{b\sigma\Psi_0} , \quad (16)$$

236 where δ_c is the effective slip-weakening distance (roughly $2D_c$ for the slip law) and
 237 $\Delta\tau_{p-r} = b\sigma\Psi_0$ is the strength loss behind the front (evolution effect). Comparing the

238 Ψ_0 -dependence of (16) and (13) shows that the scaling of R is identical to that of the
 239 entire pulse only for $p = 0$. This makes deriving a self-similar solution simplest for that
 240 case. The assumption that the fault is initially at steady state also seems less contrived
 241 than requiring a particular gradient of the ambient stress, as seems necessary for $p = 1$.
 242 In sections 4-5 we derive a self-similar solution for $p = 0$; some generalizations to other
 243 values of p are given in Appendix B.

4. Implications of self-similarity

244 Figure 2b motivates writing the normalized slip as a function of scaled distance X
 245 behind the tip; that is,

$$246 \frac{\delta(x, t)}{D_c} = f(X) , \quad X \equiv \frac{x'}{L_b} \Psi_0 , \quad (17)$$

247 where x' is the physical distance behind the tip and the time dependence is now embodied
 248 in Ψ_0 . Assuming a uniform θ_{bg} and differentiating (17) with respect to time (for details
 249 see Appendix A), the slip speed normalized by its current maximum is

$$250 \frac{V}{V_{max}} = \frac{f'}{f'_{V_m}} + f' C (X - X_{V_m}) . \quad (18)$$

251 Here $f' \equiv df/dX$, X_{V_m} is the scaled position of the maximum slip speed, f'_{V_m} is f'
 252 evaluated at X_{V_m} , and, consistent with equation (14) with $p = 0$, C characterizes the rate
 253 of acceleration to instability \dot{V}_{max} :

$$254 C \equiv \frac{\dot{V}_{max} D_c}{V_{max}^2 \Psi_0} . \quad (19)$$

255 The first term in (18) would be the sole term for a steady-state pulse; the second comes
 256 from the fact that the length scale changes with Ψ_0 . We find numerically that because of

257 the universality of the near-tip stress distribution, f'_{V_m} and X_{V_m} vary by only 5% as a/b
 258 increase from 0.8 to 0.95; for $a/b = 0.9$, $f'_{V_m} \sim 1.33$ and $X_{V_m} \sim 0.66$.

259 Although self-similarity of the slip profiles as embodied in (17) does not require $C =$
 260 constant, if the profiles of V/V_{max} are also functions of X but not time, as in Figure 2a for
 261 small-to-moderate X , then from (18) C must be independent of time. We can test this by
 262 plotting $V/(V_{max}f')$ versus X ; from (18) the result should be a line of slope C . Figure 3
 263 shows that the simulation of Figure 2 evolves to such a state over $0 < X \lesssim 50$, where the
 264 accumulated slip has reached roughly 90% of its ultimate value. That is, self-similarity
 265 of both the slip and velocity profiles is maintained over most of the pulse width but not
 266 farther from the tip. The value of C obtained from the slope is 0.0036, within a few
 267 percent of the value obtained by evaluating the right side of (19) numerically (see Section
 268 6).

269 If slip is a function of X alone, then from (2) we can write the normalized stress change
 270 as (see also Figure 2c)

$$271 \quad \frac{\Delta\tau}{b\sigma} = \Psi_0 g(X) . \quad (20)$$

272 The remainder of the derivation is somewhat cumbersome and not very illuminating, so
 273 we leave the details for Appendix A. The basic strategy is to substitute equations (18) and
 274 (20) for V and $\Delta\tau$ into equation (1) for the frictional strength to constrain θ . This requires
 275 first relating $\Delta\tau$ to τ via the background stress state, which is where the requirement of
 276 a steady-state background enters the solution. Substituting the time-derivatives of V and
 277 τ into the time-derivative of (1) then constrains $\dot{\theta}/\theta$. Requiring this $\dot{\theta}/\theta$ to be consistent
 278 with the evolution law leads finally to equation (A16), which, after retaining only the

279 dominant terms (those that multiply Ψ_0), becomes

$$280 \quad C \left(g - \frac{a}{b} \right) + \left(\frac{g'}{f'} + g + 1 - \frac{a}{b} \right) \frac{V}{V_{max}} = 0 , \quad (21)$$

281 with V/V_{max} given by (18). Along with the elasticity equation (2) relating g to f' , (21)
 282 becomes the governing equation for self-similar slip-law slip pulses with $p = 0$. The
 283 conclusions in Sections 4.1–4.5 follow directly from this, independent of the particular
 284 forms of f and g .

4.1. Spatial extent of self-similarity

285 For a constant-displacement dislocation, the stress (and hence g) varies as X^{-1} , so g'
 286 varies as X^{-2} . In the limit of large X , equation (18) becomes $V/V_{max} \approx f'/f'_{Vm} + f'CX$.
 287 In this limit, then, retaining only the (possibly) non-zero terms in (21) leads to

$$288 \quad \frac{a}{b} = \left(1 - \frac{a}{b} \right) f'X . \quad (22)$$

289 But f' must decay more rapidly than X^{-1} or the displacement will increase at least as
 290 $\ln X$, so for large X (22) implies $a/b = 0$. Therefore (21) does not satisfy the expected
 291 boundary conditions for large X . This is consistent with Figure 3, which shows that
 292 self-similarity extends over most of the pulse width but no farther.

4.2. Stress minimum

293 The stress minimum behind the tip can be determined by setting $g' = 0$ in (21), leading
 294 to

$$295 \quad g_{min} = \left(\frac{a}{b} - 1 \right) + \frac{C}{C + V_{gmin}/V_{max}} , \quad (23)$$

where V_{gmin} is the slip speed evaluated at the stress minimum. In all our simulations V_{gmin}/V_{max} is of order 1 (numerically we find it to be ~ 0.3 , regardless of the pulse style p or a/b), while C in the example in Figure 3 is 2 orders of magnitude lower. In Section 5.1 we estimate C to be $\sim 0.4(1 - a/b)^2$, implying that the second term on the right in (23) is smaller than the first by a factor of $\sim (1 - a/b)$. Thus for a/b near 1,

$$g_{min} \approx -(1 - a/b) , \quad (24)$$

explaining why $g_{min} \sim -0.1$ in Figure 2c. To the extent that $\ln(V/V_{bg})$ can be approximated as constant from V_{max} to V_{gmin} , (24) also implies that the fault is near steady-state at the stress minimum. This follows from equation (1) and the definition $g \equiv \Delta\tau/b\sigma\Psi_0$ (equation 20); for a fault initially at steady-state subjected to a constant velocity V_{max} the change in steady-state stress is $(a/b - 1)b\sigma\Psi_0$. In Appendix D we show why this stress minimum is also approximately a minimum in $\ln(V\theta/D_c)$ (Figure 1).

4.3. Dependence upon a/b

Although g_{min} varies with a/b , the fracture energy does not (equation 5). Thus larger magnitudes of g_{min} must be compensated for by smaller length scales L over which those stresses act. With $G \sim L\Delta\tau^2/\mu'$ (equation 9), $\delta \sim L\Delta\tau/\mu'$ (equation 10), and $\Delta\tau/b\sigma \propto (1 - a/b)$ (equation 24), we anticipate

$$\delta/D_c \propto (1 - a/b)^{-1} ; \quad (25)$$

$$L/L_b \propto (1 - a/b)^{-2} . \quad (26)$$

315 These scalings are properties of the analytical solution derived in Section 5. To estimate
 316 the dependence of C upon a/b requires estimates of f and g in (21).

4.4. Time to instability

317 Under the aging law, expanding nucleation zones accelerate to instability according to

$$318 \quad \frac{\dot{V}}{V^2} = \frac{C_{age}}{D_c}, \tag{27}$$

319 where the constant $C_{age} = (\pi/2)(1 - a/b)$ and V is the quasi-uniform slip speed within the
 320 interior of the nucleation zone [Rubin and Ampuero, 2005]. Neglecting elastodynamics,
 321 infinite slip speeds are reached at a finite time t^* given by

$$322 \quad t^* - t = \frac{D_c}{C_{age}V(t)}. \tag{28}$$

323 Inspection of equations (27) and (19) shows that, given comparable values of the constant,
 324 instability is reached sooner for the slip law with $p = 0$ than for the aging law. An
 325 analytic solution for equation (19) shows that in the limit of large Ψ_0 , the time remaining
 326 to instability is

$$327 \quad t^* - t \approx \frac{D_c}{C\Psi_0(t)V_{max}(t)} \tag{29}$$

328 (Appendix B). This result might be rationalized by noting that for large V_{max} , $d\Psi_0/dV_{max}$
 329 tends to zero, so Ψ_0 acts as a quasi-constant correction to C . Once C is known, $\Psi_0(t)$
 330 and $V_{max}(t)$ can be determined by solving equation (B17) numerically.

4.5. Propagation distance

331 Writing dV_{max}/dt as $(dV_{max}/dl)(dl/dt)$, where l is the position of the pulse tip, equation
 332 (19) becomes

$$333 \quad \frac{dV_{max}}{dl} \frac{dl}{dt} = \frac{C}{D_c} \Psi_0 V_{max}^2 . \quad (30)$$

334 *Ampuero and Rubin* [2008] showed that for both the aging and slip laws the propagation
 335 speed $V_{prop} = dl/dt$ satisfies

$$336 \quad V_{prop} = V_{max} \frac{L_b}{D_c} \frac{1}{f'_{Vm} \Psi_0} . \quad (31)$$

337 This is because to first order the front of the slip pulse propagates with a steady state slip
 338 profile, so that the slip speed is simply the propagation speed times the local slip gradient
 339 (with regard to equation (A6), the second term within brackets, which accounts for the
 340 sharpening of the pulse front, is less than a few percent of the first, which accounts for its
 341 steady-state translation). The slip gradient is determined largely by the near-tip strength
 342 loss $b\sigma\Psi_0$, with a/b and p having only a few percent influence on f'_{Vm} (even changing
 343 between the slip and aging laws alters f'_{Vm} by only $\sim 20\%$). Substituting (31) into (30)
 344 leads to

$$345 \quad \frac{d\Psi_0/d\bar{l}}{\Psi_0^2} = f'_{Vm} C , \quad (32)$$

346 where $\bar{l} \equiv l/L_b$. As this equation is identical in form to (27), instability (infinite Ψ_0) is
 347 reached at a finite location \bar{l}^* given by

$$348 \quad \bar{l}^* - \bar{l} = \frac{1}{f'_{Vm} C \Psi_0(\bar{l})} . \quad (33)$$

349 Note that the expression for the time to instability (29) has V_{max} in the denominator,
 350 whereas (33) has only its logarithm (in Ψ_0). This means that if a slip pulse begins at $t = 0$

351 with $V_{max} = 10^8$ m/s, then when $V_{max} = 0.1$ m/s the time remaining to instability is less
 352 than 10^{-7} of the pulse lifetime. In practical terms this means that for evaluating t^* it is
 353 immaterial whether one defines instability to occur at infinite slip speed or just elastody-
 354 namic slip speeds, a fact exploited by *Dieterich* [1994] to derive simplified expressions for
 355 earthquake aftershock rates. The same cannot be said for l^* ; the distance remaining to
 356 instability at $V_{max} = 0.1$ m/s in Figure 1a ($\Psi_0 = 23.0$) is 25% of the distance remaining
 357 when $V_{max} = 10^{-8}$ m/s ($\Psi_0 = 5.8$). This contrast with t^* is even more stark for other
 358 values of p ; for $p \geq 1/2$ instability is reached at a finite t^* but not a finite l^* (Appendix
 359 B). For example, dV_{max}/dl is constant in Figure 1f ($p = 1$), so l^* does not exist but the
 360 pulse obviously reaches elastodynamic slip speeds at a finite l .

5. Analytical approximation for a finite-width pulse

361 To evaluate (29) or (33) it is still necessary to estimate C , which controls the rate
 362 of acceleration to instability. To this end we must determine $f(X)$, $g(X)$, and their
 363 derivatives in (21). Examination of Figures 2c and 2b suggests that the slip pulses we
 364 seek to describe might reasonably be approximated as having a constant stress gradient
 365 over a finite-width pulse, with constant slip at greater distances from the tip. Given the
 366 rather abrupt onset of slip near the pulse front (50% of the total accrues over less than
 367 10% of the pulse width), a constant stress gradient is a plausible smoothing of the $1/X$
 368 singularity associated with a dislocation. Although the slip speed at large distances in
 369 Figure 2a is not zero, it is too low for significant additional displacements to accumulate
 370 prior to instability, so continued slip there does not influence the active pulse. Such a
 371 model has 4 parameters: The average stress change $\Delta\bar{\tau}$ and stress gradient $\nabla\tau$ within the

372 pulse, the pulse width $2w$, and the total displacement D . To determine these we have the
 373 following 4 constraints (for details see Appendix C):

374 (1) $K = K_c$ at $x = 0$:

$$375 \quad \frac{1}{2\pi^{1/2}} \frac{D\mu'}{w^{1/2}} - \pi^{1/2} \Delta\bar{\tau} w^{1/2} + \frac{\pi^{1/2}}{2} \nabla\tau w^{3/2} = (2\mu' b\sigma D_c \Psi_0)^{1/2} . \quad (34)$$

376 The first term on the left represents the contribution to the stress intensity factor from
 377 a fixed displacement D for $x > 2w$ and zero stress change over $0 < x < 2w$, the second
 378 the contribution from a constant (negative) stress change $\Delta\bar{\tau}$ over $0 < x < 2w$, and the
 379 third the contribution from a constant stress gradient with zero average over $0 < x < 2w$
 380 [*Broberg, 1999*]. The term on the right is K_c from (7).

381 (2) $K = 0$ at $x = 2w$:

$$382 \quad -\frac{1}{2\pi} \frac{D\mu'}{w^{1/2}} - \Delta\bar{\tau} w^{1/2} - \frac{1}{2} \nabla\tau w^{3/2} = 0 . \quad (35)$$

383 The terms on the left have the same sources as those in (34).

384 (3) Continuity of the stress gradient at $x = 2w$: The constraint $K = 0$ ensures that the
 385 stress remains finite, but permits a cusp in the stress distribution at $x = 2w$ that for the
 386 adopted friction law seems unphysical. A continuous stress gradient requires

$$387 \quad \nabla\tau = -\frac{\Delta\bar{\tau}}{2w} ; \quad (36)$$

388 that is, the difference in stress between the pulse endpoints has the same magnitude as
 389 the average stress drop.

390 (4) From (24) and (20), the stress at the tip is

$$391 \quad \Delta\tau_{min} = -b\sigma\Psi_0 \left(1 - \frac{a}{b}\right) . \quad (37)$$

392 Combining (34)–(37) leads to

$$393 \quad \frac{D}{D_c} = \frac{9}{8} \left(1 - \frac{a}{b}\right)^{-1} , \quad (38)$$

$$394 \quad g' = \frac{8\pi}{27} \left(1 - \frac{a}{b}\right)^3 , \quad (39)$$

$$395 \quad \frac{w}{L_b}\Psi_0 \equiv W = \frac{9}{8\pi} \left(1 - \frac{a}{b}\right)^{-2} , \quad (40)$$

396

397 where W is the scaled dimensionless version of w ; in units of X , the pulse width is $2W$.

398 Together with equation (24), $g_{min} = -(1 - a/b)$, this completes the solution. The slip

399 over $0 < X < 2W$ and stress for $X > 2W$ can be determined by elasticity (Appendix C).

400 For $a/b = 0.9$, (38)–(40) yield $D = 11.25D_c$, $g' = 0.93 \times 10^{-3}$, and $2W = 71.6$. For D

401 and g' these are encouragingly close to the numerical values of $\sim 12.5D_c$ and $\sim 0.9 \times 10^{-3}$

402 for the example in Figure 2. The pulse width in the numerical simulations is subjective,

403 as the slip gradient never reaches zero for large X , but from Figures 2 and 3 a value of

404 $2W \sim 70$ seems reasonable.

5.1. Rate of acceleration

405 We can solve for C in (21) by writing $g_{min} + g'X$ for g , substituting (18) and (24) for

406 V/V_{max} and g_{min} , and taking the limit $X \gg X_{Vm}$:

$$407 \quad C = \frac{1}{f'_{Vm}} \left\{ \frac{1 - g'X}{g'(1 + f'X)} - X \right\}^{-1} . \quad (41)$$

408 Because the finite pulse of Section 5 is only an approximation to (21), we cannot expect
 409 the right side of (41) to be independent of X . Nonetheless, to the extent that this
 410 approximation is valid it should vary only slightly over the central portion of the pulse.
 411 Writing $X = \beta W$, where ultimately we will choose β to be not too far from 1 (the pulse
 412 midpoint), we can write $f'(X) = (1 - a/b)f'_2(\beta)$, where the function $f'_2(\beta)$ can be evaluated
 413 from equation (C16). Substituting βW for X , $(1 - a/b)f'_2$ for f' , and (39) and (40) for g'
 414 and W , (41) becomes

$$415 \quad C = \frac{(1 - a/b)^2}{f'_{Vm}} \left[\frac{\beta f'_2 + (8\pi/9)(1 - a/b)}{3 - (9/8\pi)\beta^2 f'_2 - 2\beta(1 - a/b)} \right]. \quad (42)$$

416 This estimate is plotted as the solid line in Figure 4 for $X = W$ ($\beta = 1$; $f'_2 = 2/3$), and as
 417 the dashed line for $X = 0.5W$ ($\beta = 0.5$; $f'_2 = 3^{1/2}$), assuming $f'_{Vm} = 1.33$. The two curves
 418 are suitably similar. Note that as a/b approaches 1, C is asymptotically proportional to
 419 $(1 - a/b)^2$; $C = 0.18(1 - a/b)^2$ for $X = W$ (dotted line) and $0.23(1 - a/b)^2$ for $X = 0.5W$.
 420 Numerical values from Section 6 (red dots) are better approximated as $C \sim 0.4(1 - a/b)^2$,
 421 but equation (42) shows that the full dependence upon a/b is not so simple.

6. How robust a solution?

422 To verify that self-similar pulses with the scaling of Figure 2 are not restricted to a very
 423 limited range of a/b or Ψ_0 (see Appendix A), we sought numerical examples for other values
 424 of a/b . As the most important requirement seems to be that the pulse propagate into a
 425 region previously sliding at a uniform steady state, we prescribed initial and boundary
 426 conditions where for $x > 0$ and $t = 0$ the fault was sliding at steady state with 10^{-11} m/s,
 427 and for $x \leq 0$ and all $t \geq 0$ it was forced to slide at 10^{-9} m/s. Conceptually this might

428 bear some resemblance to nucleation at a material transition, where a locked velocity-
 429 weakening portion of the fault over $x > 0$ is loaded by creep over $x < 0$, but our primary
 430 motivation is simply to generate numerical pulses that might be analogs for the pulse-like
 431 portion of the nucleation process seen in Figure 1a.

432 Figure 5 shows examples with $a/b = 0.8, 0.9,$ and 0.95 . In each case pulse propagation
 433 for the first 4 or so snapshots is driven by the prescribed slip over $x < 0$. However, after
 434 about the 5th snapshot, or peak slip speeds in excess of $10^{-8} - 10^{-7}$ m/s, the pulses become
 435 self-driven in that they propagate with negligible additional displacement over $x < 0$. In
 436 accordance with the model of Section 5 the total slip is constant and proportional to
 437 $(1 - a/b)^{-1}$; the solid bars in Figures 5a and 5c show the expectation from equation (38).

438 We can evaluate the rate of acceleration C from equation (19) by differentiating the
 439 numerical output to obtain \dot{V}_{max} (Figure 6). Although it turns out not to be strictly
 440 constant in these simulations, C varies by only 10 – 20% for slip speeds from $10^{-5} - 1$
 441 m/s (it varies by less for the example in Figure 1a). The values at 1 m/s are 25% – 50%
 442 larger than the estimates from equation 42 (Figure 4).

443 To further assess the accuracy of the approximate self-similar solution, Figure 7 shows
 444 the last 5 slip and stress profiles from each of the numerical simulations in Figure 5, with
 445 axes scaled by $D, \Delta\tau_{min},$ and W in equations (37)–(40). The pulse width is $X/W = 2$.
 446 The self-similar solution is shown by the dashed black curve; after accounting for the
 447 scaling of the axes this solution is independent of a/b . Note that the numerical differences
 448 between the 3 values of a/b are comparable to the discrepancy between any particular
 449 a/b and the analytical solution. The largest discrepancy occurs in the stress profiles near
 450 $X/W = 0$, because the stress singularity in the analytical solution is smoothed by the

451 near-tip strength loss in the numerical simulations. We can make an improved estimate
 452 of the actual stress minima by evaluating the second term on the right of equation (23),
 453 which represents a higher-order correction to the value $-(1 - a/b)$ assumed analytically.
 454 As was noted in section 4.2, this correction is roughly $(1 - a/b)$ times the first term, so
 455 higher-order corrections would imply scaled stress minima in Figure 7b of roughly -0.8 ,
 456 -0.9 , and -0.95 for $a/b = 0.8, 0.9$, and 0.95 , respectively. While these are close to the
 457 actual values, one might expect (23) to be “exact” in the sense that it assumes only self-
 458 similarity and not any particular form for f and g . Inserting into (23) the relevant values
 459 from the numerical simulations for each a/b , the expected minima in Figure 7b are -0.78 ,
 460 -0.88 , and -0.978 . That the actual values are not identical to these is symptomatic of
 461 these slip pulses being not exactly self-similar.

462 Because the length of the slip-weakening region is nearly independent of a/b , that region
 463 occupies a larger fraction of the pulse as a/b (and hence W) decreases. For $a/b = 0.8$
 464 this begins to impact the small-scale yielding approximation, which is presumably why
 465 the discrepancy between the numerical and analytical slip profiles for $X/W \lesssim 1$ is largest
 466 for this case (Figure 7a).

467 To assess the importance of the assumption of a steady-state fault, Figure 8 shows (from
 468 left to right) simulations with $V_{bg}\theta_{bg}/D_c = 4, 2, 1.4, 1$ (steady state), and 0.8 . The slip
 469 magnitudes in these cases appear to be approaching their self-similar values, both with
 470 increasing Ψ_0 and with increasing proximity of $V_{bg}\theta_{bg}/D_c$ to steady state. Qualitatively
 471 this is consistent with the diminishing importance of the $\ln(V_{bg}\theta_{bg}/D_c)$ term in equation
 472 (A16), which was neglected in the self-similar solution. The propagation distances deviate
 473 more from the $p = 0$ self-similar solution than does the total slip, but as could have been

474 anticipated this distance is shorter for $V_{bg}\theta_{bg}/D_c > 1$ (larger ambient stress) and longer
 475 for $V_{bg}\theta_{bg}/D_c < 1$. Because the propagation speed at a given V_{max} is essentially fixed by
 476 Ψ_0 (equation 31), a larger $d\ln(V_{max})/dl$ implies a larger $d\ln(V_{max})/dt$.

477 Figure 8 provides a qualitative explanation of Figure 7 of *Ampuero and Rubin* [2008],
 478 where an effective $V_{bg}\theta_{bg}/D_c$ of ~ 2 was reached via heterogeneous initial conditions. For
 479 each of $a/b = 0.8, 0.9, \text{ and } 0.95$ in that figure the total slip is perhaps 75% of the $p = 0$
 480 self-similar estimate, while the propagation distance is less than half that estimate.

6.1. Extrapolation to natural faults

481 Even assuming that the slip law accurately describes state evolution in the presence of
 482 high temperatures and pore fluids, the pulses described here might operate only within
 483 a limited velocity range or be bypassed entirely, depending upon the ambient conditions.
 484 To place some bounds on $V_{bg}\theta_{bg}/D_c$, note that during rapid (elastodynamic) slip the fault
 485 is near steady state because the slip speed is quasi-constant for slip distances much larger
 486 than D_c . Immediately following the event the fault slows dramatically, so $V\theta/D_c \ll 1$ and
 487 $\dot{\theta} > 1$ (equation 4). Because for $V\theta/D_c \ll 1$ the strength increase due to state evolution is
 488 very small for the slip law, and only logarithmic with time for the aging law, the increase
 489 in θ alone cannot balance a quasi-linear increase in loading stress. Thus V increases as
 490 well as θ (equation 1), and $V\theta/D_c$ increases during the interseismic period. Self-driven
 491 nucleation, on the other hand, requires both increasing slip speed and decreasing stress.
 492 From (1) this implies a decreasing θ , requiring $V\theta/D_c > 1$. Thus nucleation is associated
 493 with the passage of the fault through steady state from below, as is true of both nucleation
 494 zones in Figure 1.

495 Under 2 circumstances this increasing $V\theta/D_c$ and localization can persist until insta-
496 bility, bypassing pulse formation entirely: For a/b well below lab values [*Ampuero and*
497 *Rubin*, 2008], and for rapidly increasing stresses, such as occur following a nearby earth-
498 quake [*Kaneko and Lapusta*, 2008], or when creep fronts collide, for example within an
499 asperity loaded by creep of the surroundings [*Chen and Lapusta*, 2009]. However, for lab
500 values of a/b and low stressing rates, the stiffness of such a localized zone is too large to
501 allow instability, causing $V\theta/D_c$ to decrease toward steady state and the nucleation zone
502 to expand. The slip speed at the onset of expansion is sensitive to the initial conditions,
503 in a way that we cannot yet predict quantitatively. All we can say at present is that in
504 the simulations carried out thus far, the pulse develops at slip speeds that are orders of
505 magnitude below elastodynamic. Unpublished numerical simulations demonstrate that
506 this occurs also in 3-D, where the pulse may emanate from either the mode-II or the
507 mode-III margins of the initially localized nucleation zone.

508 Thus when a pulse develops, it emanates from a region that is somewhat above steady
509 state (or localization would not have occurred), but not too far above steady state (or
510 localization would have continued), as in Figure 1. We would not expect the adjacent fault
511 to be farther above steady state or localization would have first occurred there. Conceiv-
512 ably the adjacent fault could be far below steady state, but given that it is contiguous
513 with the original nucleation zone and was being stressed during that nucleation, this would
514 require a significant and abrupt change in material properties or ambient stress. Barring
515 that, the fault into which the pulse propagates seems most likely to be slightly closer to
516 steady state than the original zone of localization, as in Figure 1. Thus the range of initial
517 conditions explored in Figure 8 seems appropriate.

518 At high slip speed, the slip pulses described here will be limited by the onset of elasto-
 519 dynamics if not sooner. Possibilities for “sooner” include pore fluid pressurization [*Segall*
 520 *and Rice*, 2006] or a high-speed cut-off to the evolution of state in the presence of hot
 521 pore fluids [*Nakatani and Scholz*, 2006]. Based on the acceleration-in-place, aging-law
 522 nucleation model of *Dieterich* [1992], Segall and Rice suggested that thermal pressuriza-
 523 tion might dominate rate-and-state weakening at slip speeds as low as 10^{-5} m/s. Given
 524 how different these slip pulses are from Dieterich’s model, however, with relatively little
 525 total slip occurring in regions that were only recently added to the pulse front, it is worth
 526 revisiting this issue. Nakatani and Scholz propose that under hydrothermal conditions,
 527 pressure solution creates relatively large, low-stress contact points that under stationary
 528 contact increase their area only slowly (compared to dislocation motion at high-stress con-
 529 tacts in room-temperature experiments). When the characteristic time for a significant
 530 increase in contact area is larger than the contact age $\sim D_c/V$, evolution is not significant.
 531 The implications of such a constitutive law for nucleation on deformable faults have yet
 532 to be assessed.

7. Comparison to aging-law nucleation

7.1. Time to instability

533 For lab values of a/b and low stressing rates, nucleation zones following either the
 534 aging or the slip evolution law undergo expansion while $V\theta/D_c$ in the interior remains
 535 slightly above steady state. The difference is that this expansion takes the form of
 536 slip pulses under the slip law and cracks under the aging law. For the aging law in
 537 the crack expansion regime the time to instability is given by equation (28) with $C_{age} =$
 538 $(\pi/2)(1-a/b)$ [*Rubin and Ampuero*, 2005]. Comparison to equation (29), with $f'_{Vm} \sim 1.33$

539 and $C \sim 0.4(1 - a/b)^2$, shows that instability occurs sooner for the slip law only if

$$540 \quad \Psi_0 \gtrsim \frac{4}{1 - a/b} \frac{V^{age}}{V_{max}^{slip}}, \quad (43)$$

541 where V^{age} is the quasi-uniform slip speed within the interior of the aging-law nucleation
 542 zone. Given that in practical terms the maximum Ψ_0 is bounded by the onset of elasto-
 543 dynamics, (43) implies that for $V^{age} = V_{max}^{slip}$, instability occurs sooner for the aging law if
 544 a/b is close to 1. This results from the different dependencies of (28) and (29) on $1 - a/b$,
 545 and it might seem surprising, given the smaller fracture energy implied by the slip law.
 546 However, *Ampuero and Rubin* [2008, equation B13] noted that for aging-law nucleation
 547 zones the ratio of V in the interior to V_{max} at the margins is roughly proportional to
 548 $1 - a/b$, so that if a comparison is made at the same V_{max} the dependency of the 2 laws
 549 on a/b is approximately the same. Inserting into (28) their numerical values for the aging
 550 law of $V_{max}/V \sim 6$ for $a/b = 0.9$ and $V_{max}/V \sim 14$ for 0.95, instability occurs sooner for
 551 the slip law if $\Psi_0 \gtrsim 6$, or $V_{max}/V_{bg} \gtrsim 400$. This comprises most or all of the region where
 552 C_{age} in (28) is expected to be accurate.

7.2. Nucleation zone size

553 In the crack expansion regime the asymptotic nucleation length $2L_\infty$ for the aging law
 554 is

$$555 \quad \frac{2L_\infty}{L_b} = \frac{2}{\pi}(1 - a/b)^{-2} \quad (44)$$

556 [*Rubin and Ampuero*, 2005]. Given that C in (33) is roughly proportional to $(1 - a/b)^2$,
 557 this length and the slip-law propagation distance have roughly the same dependency
 558 upon a/b . If we take $V_{bg} = 10^{-11}$ m/s, and assume for example that a pulse develops at

559 $V_{max} = 10^{-8}$ m/s and reaches elastodynamic speeds at $V_{max} = 10^{-2}$ m/s, then from (33)
 560 the propagation distance is roughly 1/6 the aging-law nucleation length $2L_\infty$. For a fault
 561 initially above steady state that propagation distance can be significantly less (by more
 562 than a factor of 2 for $V_{bg}\theta_{bg}/D_c = 2$ in Figure 8). For the aging law, being above steady-
 563 state can also reduce the nucleation size at elastodynamic speeds, but the effect is much
 564 more modest. For example, in Figure 1e of *Rubin and Ampuero* [2005], $V_{bg}\theta_{bg}/D_c \sim 3$
 565 and the nucleation length at dynamic slip speeds is $\sim 75\%$ of $2L_\infty$.

7.3. Detectability

566 The disparity between the two laws is even greater when one considers the size of the
 567 actively slipping region. While this can approach the full $2L_\infty$ for the aging law, for
 568 the slip law the slip speed has already dropped below $0.1V_{max}$ by the pulse half-width
 569 w (Figure 2a, where $w = 32X$). From equations (40) and (44) the ratio $2L_\infty/w \sim 2\Psi_0$,
 570 which can easily reach a value of 40 at elastodynamic speeds (see also Figure 2 of *Ampuero*
 571 *and Rubin* [2008]). Thus the seismic signal from the final stages of nucleation is expected
 572 to be much smaller for the slip law than for the aging law. Unpublished simulations show
 573 that in 3-D this difference would be even greater, because while the aging-law nucleation
 574 length is roughly $2L_\infty$ in both dimensions, for the slip law the length in the direction
 575 orthogonal to the 2-D simulations presented here is several times smaller than L_∞ .

7.4. Total slip

576 Integrating (27) with $C_{age} = (\pi/2)(1 - a/b)$, the slip that accumulates between slip
 577 speeds V_1 and V_2 for the aging law is

$$578 \quad \frac{\delta}{D_c} = \frac{2}{\pi}(1 - a/b)^{-1} \ln \frac{V_2}{V_1}. \quad (45)$$

579 As this has the same dependence upon a/b as does D for the slip law, we can ask how
580 large a velocity increase is required for the aging law to accumulate the total slip of the
581 slip-law pulse. Setting (45) equal to (38) leads to $\ln(V_2/V_1) = 9\pi/16$, or $V_2/V_1 = 5.9$.
582 Thus the total slip during nucleation, which accrues over many orders of magnitude in V ,
583 is many times larger for the aging law than for the slip law.

7.5. (Lack of) implications for elastodynamic slip pulses

584 Given their form, it is tempting to think of the slip pulses described here as potentially
585 “jump-starting” elastodynamic slip pulses during earthquake rupture. But this seems not
586 to be the case. Despite the fact that all the action appears to be happening at the pulse
587 front, the region behind the front is still accelerating, just more slowly. When the maxi-
588 mum slip speed is large enough that acceleration is limited by elastodynamics, this allows
589 slower regions behind the front to also accelerate to elastodynamic speeds. In simulations
590 that include radiation damping as an approximation to full elastodynamics [Rice, 1993],
591 this leads to bilateral ruptures emanating from the region where the tip first reached ra-
592 diation damping speeds (Figure 9). Although they differ in detail, fully elastodynamic
593 simulations share this property (Yoshihiro Kaneko and Jean-Paul Ampuero, ms. in prepa-
594 ration). Both the observed quasi-static pulses and the lack of elastodynamic pulses are
595 consistent with the results of Perrin *et al.* [1995], who found that the slip evolution law
596 could not give rise to steady-state slip pulses with a slip speed that decreased to zero at
597 some finite distance behind the pulse front. Neither their steady-state nor their zero slip
598 speed criterion is met by the quasi-static pulses we describe, although in practical terms
599 the slip speeds we observe well behind the pulse front are negligibly small.

8. Conclusions

600 We have derived a self-similar solution for one of 3 styles of slip pulses observed in
 601 numerical simulations of earthquake nucleation on faults obeying the slip law for state
 602 evolution. The solution is for faults that are initially at steady state, but remains useful
 603 for initial conditions that depart modestly from this. The stress drop, total slip, and
 604 pulse width vary with a/b as $(1 - a/b)$, $(1 - a/b)^{-1}$, and $(1 - a/b)^{-2}$, respectively. With
 605 increasing $\Psi_0 = \ln(V_{max}\theta_{bg}/D_c)$ the stress drop, total slip, and pulse width vary as Ψ_0 , Ψ_0^0 ,
 606 and Ψ_0^{-1} . The dependence of the stress drop, slip, and length scales with $(1 - a/b)$ is the
 607 same as for nucleation under the aging evolution law, making direct comparison rather
 608 straightforward. The same is not true of the variation with Ψ_0 . In particular, the continual
 609 sharpening of the pulse front under the slip law bears no similarity to nucleation under the
 610 aging law, and would make the moment rate at the final stages of quasi-static nucleation
 611 much smaller for the slip law. This difference ultimately derives from the smaller increase
 612 in fracture energy with slip speed under the slip law. If existing lab experiments are a
 613 legitimate guide to natural faults, then the slip law is a more appropriate constitutive law
 614 for nucleation than is the aging law. However, we may be far from understanding the
 615 appropriate constitutive law for natural faults.

Appendix A: Self-similarity with $p=0$

616 Motivated by the scaling apparent in Figure 2, we begin by assuming

$$617 \quad \frac{\delta}{D_c} = f(X), \quad X \equiv \frac{x'}{L_b}\Psi_0; \quad (A1)$$

$$618 \quad \frac{V}{V_{max}} = g(X); \quad (A2)$$

620 where x' is distance behind the pulse tip and $\Psi_0 \equiv \ln(V_{max}\theta_{bg}/D_c)$. For a pulse propagat-
 621 ing into a region initially sliding at a uniform background state $d\theta_{bg}/dt = 0$, so

$$622 \quad \frac{dX}{dt} = \frac{d(x'/L_b)}{dt} \Psi_0 + \frac{x'}{L_b} \frac{\dot{V}_{max}}{V_{max}}; \quad (A3)$$

$$623 \quad \frac{V}{D_c} = \frac{df}{dX} \frac{dX}{dt} = f' \left[\frac{V_{prop}}{L_b} \Psi_0 + X \frac{\dot{V}_{max}}{V_{max} \Psi_0} \right]; \quad (A4)$$

625 where we have equated dx'/dt with the pulse propagation velocity V_{prop} , and have written
 626 f' for df/dX and \dot{V}_{max} for dV_{max}/dt . Multiplying by D_c/V_{max} ,

$$627 \quad \frac{V}{V_{max}} = f' \left[\frac{V_{prop}}{V_{max}} \frac{D_c}{L_b} \Psi_0 + X \frac{\dot{V}_{max} D_c}{V_{max}^2 \Psi_0} \right]. \quad (A5)$$

628 At $V = V_{max}$,

$$629 \quad 1 = f'_{V_m} \left[\frac{V_{prop}}{V_{max}} \frac{D_c}{L_b} \Psi_0 + X_{V_m} \frac{\dot{V}_{max} D_c}{V_{max}^2 \Psi_0} \right], \quad (A6)$$

630 where f'_{V_m} and X_{V_m} are the values of f' and X evaluated where $V = V_{max}$. Substitution
 631 back into (A5) yields

$$632 \quad \frac{V}{V_{max}} = f' \left[\frac{1}{f'_{V_m}} + C(X - X_{V_m}) \right]; \quad C \equiv \frac{\dot{V}_{max} D_c}{V_{max}^2 \Psi_0}. \quad (A7)$$

633 With V/V_{max} a function of X only (equation A2), C must be constant.

634 In what follows we will also need expressions for \dot{V}/V and $\dot{\tau}$. When the pulse slip speed
 635 is large enough that the background stressing rate is irrelevant, $\dot{\tau} = \dot{\Delta}\tau$. Differentiating
 636 (18) and (20) and applying the chain rule as above,

$$637 \quad \frac{\dot{V}}{V} = \frac{V_{max}}{D_c} \left[C(1 + \Psi_0) + \frac{f''}{(f')^2} \frac{V}{V_{max}} \right]; \quad (A8)$$

$$\frac{\dot{\tau}}{b\sigma} = \Psi_0 \frac{V_{max}}{D_c} \left[\frac{g'}{f'} \frac{V}{V_{max}} + Cg \right]. \quad (\text{A9})$$

Thus far we have made use only of the statement of self-similarity (equations A1 and A2) in the derivation of equations (A8) and (A9), and a general statement of elasticity in deriving (20). But from the friction law, specifying $\Delta\tau$ and V places constraints on θ .

From (1) we have

$$\Delta\tau \equiv \tau - \tau_{bg} = a\sigma \ln \frac{V}{V_{bg}} + b\sigma \ln \frac{\theta}{\theta_{bg}}, \quad (\text{A10})$$

where by V_{bg} and θ_{bg} we imply values prior to any significant perturbation from the approaching slip pulse. Manipulating the logarithms in (A10) leads to

$$\ln \frac{V\theta}{D_c} = \frac{\Delta\tau}{b\sigma} + \left(1 - \frac{a}{b}\right) \left[\ln \frac{V_{max}}{V_{bg}} + \ln \frac{V}{V_{max}} \right] + \ln \frac{V_{bg}\theta_{bg}}{D_c}. \quad (\text{A11})$$

If the pulse propagates into a region at steady-state the last term on the right is zero, but we retain it for now. Substituting into (A11) the kinematic description of $\Delta\tau$ from (20),

$$\ln \frac{V\theta}{D_c} = \Psi_0 \left[g + \left(1 - \frac{a}{b}\right) \right] + \left(1 - \frac{a}{b}\right) \ln \frac{V}{V_{max}} + \frac{a}{b} \ln \frac{V_{bg}\theta_{bg}}{D_c}. \quad (\text{A12})$$

In addition to the constraint on $\ln(V\theta/D_c)$ from (A12), differentiating (1) places a constraint on $\dot{\theta}/\theta$. Starting with

$$\dot{\tau} = a\sigma \frac{\dot{V}}{V} + b\sigma \frac{\dot{\theta}}{\theta} \quad (\text{A13})$$

and inserting the kinematic constraints on \dot{V}/V and $\dot{\tau}$ from (A8) and (A9),

$$\frac{\dot{\theta}}{\theta} = \Psi_0 \frac{V_{max}}{D_c} \left[C \left(g - \frac{a}{b} \right) + \frac{g'}{f'} \frac{V}{V_{max}} \right] - \frac{a}{b} \frac{V_{max}}{D_c} \left[C + \frac{f''}{(f')^2} \frac{V}{V_{max}} \right]. \quad (\text{A14})$$

656 We can now insist that this $\dot{\theta}/\theta$, obtained by combining the frictional strength with the
 657 assumption of self-similarity, be consistent with the state evolution law. Substituting
 658 equation (A12) for $\ln(V\theta/D_c)$ into the slip law (equation 4),

$$659 \quad \frac{\dot{\theta}}{\theta} = -\frac{V}{D_c} \left\{ \Psi_0 \left[g + \left(1 - \frac{a}{b} \right) \right] + \left(1 - \frac{a}{b} \right) \ln \frac{V}{V_{max}} + \frac{a}{b} \ln \frac{V_{bg}\theta_{bg}}{D_c} \right\}. \quad (\text{A15})$$

660 Finally, equating (A14) with (A15) leads to

$$661 \quad \Psi_0 \left[C \left(g - \frac{a}{b} \right) + \frac{g'}{f'} \frac{V}{V_{max}} \right] - \frac{a}{b} \left(C + \frac{f''}{(f')^2} \frac{V}{V_{max}} \right) \\
 662 \quad = -\Psi_0 \left[g + \left(1 - \frac{a}{b} \right) \right] \frac{V}{V_{max}} - \left(1 - \frac{a}{b} \right) \frac{V}{V_{max}} \ln \left(\frac{V}{V_{max}} \right) \\
 663 \quad - \frac{a}{b} \frac{V}{V_{max}} \ln \left(\frac{V_{bg}\theta_{bg}}{D_c} \right). \quad (\text{A16}) \\
 664$$

665 Equation (A16) has the form $\Psi_0 A_1(X) + B_1(X) = \Psi_0 A_2(X) + B_2(X)$, where the left
 666 side comes from the combination of self-similarity and the frictional strength, and the
 667 right side from the combination of self-similarity and the evolution law. Two interpreta-
 668 tions seem consistent with Figure 2. The first is that there is a self-similar solution that
 669 satisfies (A16) exactly, and toward which the numerical simulation evolves. This requires
 670 $A_1 = A_2$ and $B_1 = B_2$. The second interpretation is that only $A_1 = A_2$, and that the
 671 numerical simulation approaches self-similarity more and more closely as Ψ_0 increases and
 672 the $\Psi_0 A(X)$ terms dominate (for a fault initially at steady state, $\Psi_0 = 7$ for a velocity
 673 jump of 3 orders of magnitude and 20 for a jump of 9 orders of magnitude).

674 For the simulation in Figure 2 the numerical results show that within the strongly
 675 weakening region behind the pulse tip ($X \lesssim 4$), the $\Psi_0 A(X)$ terms dominate and to
 676 within several percent $A_1 \sim A_2$. But although these terms still dominate over $X \gtrsim 5$, it
 677 is only by a factor of 2 or so even for relatively large Ψ_0 , and in this region both $A_1 \sim A_2$

678 and $B_1 \sim B_2$. For $X \lesssim 4$ the (small) $B(X)$ terms are far from equal, but their difference
 679 nearly cancels the (small) difference between the $\Psi_0 A(X)$ terms. This near-cancellation
 680 persists for $X \gtrsim 4$ as well. Thus, the full equation (A16) is satisfied to greater accuracy
 681 than either $A_1 = A_2$ or $B_1 = B_2$. This seemed to raise the possibility that the self-
 682 similarity observed in Figure 2 is limited to a particular range of Ψ_0 , or perhaps even a
 683 particular range of a/b . However, Figure 5 demonstrates that this self-similarity is not so
 684 fragile. As $A_1 \sim A_2$ everywhere within the pulse but $B_1 \neq B_2$ for $X \lesssim 4$, we set $A_1 = A_2$
 685 to derive equation (21) in the main text.

Appendix B: Generalized self-similarity

686 We noted in Section 3 that only for $p = 0$ is the scaling of slip within the near-tip region
 687 the same as that within the bulk of the pulse. Here we develop some results for $p \neq 0$.
 688 Guided by the numerical simulations of *Ampuero and Rubin* [2008], we generalize (A1)–
 689 A2) by hypothesizing self-similar solutions that on the scale of the pulse width, outside
 690 the near-tip region, satisfy

$$691 \quad \frac{\delta}{D_c} = \Psi_0^p f(X) , \quad X \equiv \frac{x'}{L_b} \Psi_0^{(1-2p)} ; \quad (B1)$$

$$692 \quad \frac{V}{V_{max}} = \Psi_0^{-p} h(X) . \quad (B2)$$

694 Examples satisfying (B1) and (B2) with $p = 1/2$ and 1 are shown in Figure B1. Note that
 695 V_{max} is the global maximum slip speed, which occurs in the near-tip region and which for
 696 $p \neq 0$ exceeds the maximum of the self-similar V in (B2).

697 Evaluating dX/dt and df/dt as in (A3) and (A4), the generalization of (A5) (still
698 neglecting $d\theta_{bg}/dt$ in comparison to dV_{max}/dt) is

$$699 \quad \frac{V}{V_{max}} = \Psi_0^{-p} \left\{ f' \left[\frac{V_{prop}}{V_{max}} \frac{D_c}{L_b} \Psi_0 + (1 - 2p)CX \right] + pfC \right\} , \quad (\text{B3})$$

700 where

$$701 \quad C \equiv \frac{\dot{V}_{max}}{V_{max}^2} \frac{D_c}{\Psi_0^{(1-2p)}} . \quad (\text{B4})$$

702 *Ampuero and Rubin* [2008] showed that for all p the near-tip scaling satisfies

$$703 \quad \frac{V_{prop}}{V_{max}} \frac{D_c}{L_b} \Psi_0 = \text{const} \equiv \alpha , \quad (\text{B5})$$

704 so from (B3)

$$705 \quad \frac{V}{V_{max}} = \Psi_0^{-p} \{ f' [\alpha + (1 - 2p)CX] + pfC \} . \quad (\text{B6})$$

706 Thus self-similarity of V as in (B2) requires constant C , as verified by our simulations
707 (Figure B2).

708 Because the maximum V in the self-similar solution does not match the global V_{max} ,
709 there is no trivial counterpart of (A6) or (A16). We can nevertheless obtain the following
710 general results:

711 Stress drop:

$$712 \quad \frac{\Delta\tau}{b\sigma} = \Psi_0^{(1-p)} g(X) . \quad (\text{B7})$$

Propagation distance:

$$p \neq 1/2 : \quad \Delta\bar{l} = \frac{1}{C f'_{Vm}} \frac{[\Psi_0(\bar{l}_1)]^{-1+2p} - [\Psi_0(\bar{l}_2)]^{-1+2p}}{1 - 2p} ; \quad (\text{B8})$$

$$p = 1/2 : \quad \Delta\bar{l} = \frac{1}{C f'_{Vm}} \ln \frac{\Psi_0(\bar{l}_2)}{\Psi_0(\bar{l}_1)} ; \quad (\text{B9})$$

713 where $\Delta \bar{l} = (l_2 - l_1)/L_b$, with l the location of the pulse front. The derivation follows
 714 that in Section 4.5. Only for $p < 1/2$ do the quasi-static equations give rise to infinite
 715 slip speeds at a finite l .

716 Remaining time to instability:

$$717 \quad p = 0 : \quad t^* - t = \frac{D_c}{CV_{max}(t)\Psi_0(t)} ; \quad (B10)$$

$$718 \quad p = 1/2 : \quad t^* - t = \frac{D_c}{CV_{max}} ; \quad (B11)$$

$$719 \quad p = 1 : \quad t^* - t = (1 + \Psi_0) \frac{D_c}{CV_{max}} ; \quad (B12)$$

720

721 where t^* is the time of instability. To derive (B10), for example, write V_{bg} for D_c/θ_{bg} in
 722 equation (19) to obtain

$$723 \quad \frac{\dot{V}_{max}}{V_{max}^2 \ln(V_{max}/V_{bg})} = \frac{C}{D_c} . \quad (B13)$$

724 This has the analytical solution

$$725 \quad \text{Ei} \left[-\ln \left(\frac{V_{max}(t)}{V_{bg}} \right) \right] - \text{Ei} \left[-\ln \left(\frac{V_{max}(0)}{V_{bg}} \right) \right] = \frac{C}{D_c} V_{bg} t , \quad (B14)$$

726 where the exponential integral function Ei is defined as

$$727 \quad \text{Ei}(x) \equiv - \int_{-x}^{\infty} \frac{e^{-t} dt}{t} . \quad (B15)$$

728 For large x , $\text{Ei}(x) \sim e^x/x$, so $\text{Ei}[-\ln(x)] \sim -1/x \ln(x)$. This leads, for $\ln[V_{max}(0)/V_{bg}] =$
 729 $\Psi_0(0) \gg 1$ and $t \geq 0$, to (B10), with

$$730 \quad t^* = \frac{D_c}{CV_{max}(0)\Psi_0(0)} . \quad (B16)$$

731 Combining (B16) with (B10), and recalling that $\Psi_0 \equiv \ln(V_{max}\theta_{bg}/D_c)$, the time history
 732 of V_{max} and Ψ_0 can be determined from the transcendental equation

$$733 \quad V_{max}(t)\Psi_0(t) = \frac{V_{max}(0)\Psi_0(0)}{1 - t\frac{C}{D_c}V_{max}(0)\Psi_0(0)} , \quad (\text{B17})$$

734 using the estimate of C from equation (42).

735 Dependence upon a/b : Unlike the case $p = 0$, we have no analytical results for the
 736 dependence of the slip pulse attributes on a/b for $p = 1/2$ or 1. This can be traced to
 737 the lack of an equation equivalent to (24) for the stress minimum behind the tip. For all
 738 p it seems that the stress minimum is close to steady-state with a slip speed near V_{max}
 739 (Appendix D); this is the constraint that led to equation (15). We can also write (B7) as

$$740 \quad \frac{\Delta\tau_{min}}{b\sigma} = \Psi_0^{(1-p)}C_1\left(\frac{a}{b}, p\right) , \quad (\text{B18})$$

741 where the constant C_1 depends upon a/b and p . Equating (B18) with (15) leads to

$$742 \quad C_1\left(\frac{a}{b}, p\right) = \left(\frac{a}{b} - 1\right)\Psi_0^p - \frac{a}{b}\frac{\Psi_{bg}}{\Psi_0^{(1-p)}} . \quad (\text{B19})$$

743 For $p = 0$ and $\Psi_{bg} = 0$ this yields $C_1 = (a/b - 1)$, so (B19) is an alternate path to
 744 equation (24), the approximation to (23) that was used in obtaining the analytical self-
 745 similar solution. Equation (23), which takes full account of self-similarity between the
 746 pulse tip and the stress minimum, can then be thought of as a second-order correction to
 747 this. For the other p (B19) becomes

$$748 \quad \Psi_{bg} = -\frac{(1 - a/b)\Psi_0 + C_1\Psi_0^{1/2}}{a/b} , \quad p = 1/2 ; \quad (\text{B20})$$

$$749 \quad \Psi_{bg} = -\frac{(1 - a/b)\Psi_0 + C_1}{a/b} , \quad p = 1 . \quad (\text{B21})$$

750

751 Thus, equation (B19) emphasizes the point that the pulse style is dependent upon the
 752 ambient conditions along the fault. For $p = 1$, (B21) is permissive of but does not require
 753 that both Ψ_{bg} and Ψ_0 vary linearly with X , as seems to be approximately the case in
 754 Figure 1. However, for both $p = 1/2$ and $p = 1$, additional information is needed to relate
 755 the unknowns C_1 and $\Psi_{bg}(X)$.

756 Empirically, we find that the numerical simulations for $p = 1/2$ seem to show similar
 757 dependencies on a/b as for $p = 0$. For $p = 1/2$, C is even closer to proportional to
 758 $(1 - a/b)^{-2}$ than is the case for $p = 0$ (Figure B2). The same simulations indicate that
 759 the total slip, at a given Ψ_0 , is approximately proportional to $(1 - a/b)^{-1}$, although not as
 760 precisely as for $p = 0$, and the pulse width, although difficult to identify precisely, varies
 761 roughly as $(1 - a/b)^{-2}$ [Ampuero and Rubin, 2008, Figure 8b].

Appendix C: Notes on the finite-width pulse solution

762 We approximate the finite-width pulse as a crack with a constant stress gradient over
 763 $0 < x < 2w$, zero slip over $-\infty < x < 0$, and constant slip D over $2w < x < \infty$ (Figure
 764 C1). Our strategy is to superpose the following 3 fundamental solutions to obtain the
 765 desired boundary conditions. For convenience we introduce the coordinate transformation
 766 $\bar{x} = (x - w)/w$, so $-1 \leq \bar{x} \leq 1$ corresponds to $0 \leq x \leq 2w$.

767 **(1) Zero slip over $\bar{x} \leq -1$, constant slip D over $\bar{x} \geq 1$, zero stress over $|\bar{x}| < 1$:**

768 The slip and slip gradient for $|\bar{x}| < 1$ are

$$769 \quad \delta = \frac{D}{\pi} \left(\frac{\pi}{2} + \sin^{-1} \bar{x} \right) , \tag{C1}$$

$$770 \quad \frac{d\delta}{dx} = \frac{1}{\pi} \frac{D}{w} \frac{1}{\sqrt{1 - \bar{x}^2}} \tag{C2}$$

772 [*Broberg, 1999, Section 4.4*]. The stress over $|\bar{x}| > 1$, determined via the same techniques
 773 or by inserting (C2) into (2), is

$$774 \quad \tau = -\frac{\mu' D}{2\pi w} \frac{1}{\sqrt{\bar{x}^2 - 1}} \frac{\bar{x}}{|\bar{x}|} . \quad (\text{C3})$$

775 **(2) Zero slip over $|\bar{x}| \geq 1$, uniform (negative) stress $\Delta\bar{\tau}$ over $|\bar{x}| < 1$:**

$$776 \quad \delta = -2w \frac{\Delta\bar{\tau}}{\mu'} \sqrt{1 - \bar{x}^2} , \quad |\bar{x}| < 1 ; \quad (\text{C4})$$

$$777 \quad \frac{d\delta}{dx} = 2 \frac{\Delta\bar{\tau}}{\mu'} \bar{x} \frac{1}{\sqrt{1 - \bar{x}^2}} , \quad |\bar{x}| < 1 ; \quad (\text{C5})$$

$$779 \quad \tau = -\Delta\bar{\tau} \left[\frac{|\bar{x}|}{\sqrt{\bar{x}^2 - 1}} - 1 \right] , \quad |\bar{x}| > 1 . \quad (\text{C6})$$

781 **(3) Zero slip over $|\bar{x}| \geq 1$, $\tau = \nabla\tau\bar{x}$ over $|\bar{x}| < 1$:** From *Secor and Pollard [1975]*,

$$782 \quad \delta = -\frac{\nabla\tau w}{\mu'} w \bar{x} \sqrt{1 - \bar{x}^2} , \quad |\bar{x}| < 1 ; \quad (\text{C7})$$

$$783 \quad \frac{d\delta}{dx} = \frac{\nabla\tau w}{\mu'} \frac{2\bar{x}^2 - 1}{\sqrt{1 - \bar{x}^2}} , \quad |\bar{x}| < 1 ; \quad (\text{C8})$$

$$785 \quad \tau = \nabla\tau w \left[\frac{1 - 2\bar{x}^2}{2\sqrt{\bar{x}^2 - 1}} + |\bar{x}| \right] \frac{\bar{x}}{|\bar{x}|} , \quad |\bar{x}| > 1 . \quad (\text{C9})$$

787 The slip contribution is negative for $\bar{x} > 0$.

788 To satisfy the boundary conditions at $x = 2w$ (or $x = 0$) we write $\bar{x} = 1 + \bar{r}$ (or
 789 $\bar{x} = -1 - \bar{r}$), and examine the stresses as $\bar{r} \rightarrow 0^+$. For $\bar{x} \geq 1$, summing the 3 contributions
 790 leads to

$$791 \quad \tau = -\frac{\mu' D}{2\pi w} \frac{1}{\sqrt{\bar{r}}\sqrt{2 + \bar{r}}} - \Delta\bar{\tau} \left[\frac{1 + \bar{r}}{\sqrt{\bar{r}}\sqrt{2 + \bar{r}}} - 1 \right] + \nabla\tau w \left[-\frac{1 + 4\bar{r} + 2\bar{r}^2}{2\sqrt{\bar{r}}\sqrt{2 + \bar{r}}} + 1 + \bar{r} \right] . \quad (\text{C10})$$

792 In the limit $\bar{r} \rightarrow 0$, and substituting r/w for \bar{r} ,

$$793 \quad \tau = \left[-\frac{D\mu'}{2\pi} w^{-1/2} - \Delta\bar{\tau} w^{1/2} - \frac{\nabla\tau}{2} w^{3/2} \right] \frac{1}{\sqrt{2r}} . \quad (\text{C11})$$

794 Requiring finite stresses at $x = 2w$ means that the bracketed terms sum to zero; as they
 795 multiply $(2r)^{-1/2}$ these are (except for a factor of $\pi^{1/2}$) the respective stress intensity
 796 factors for the 3 loading styles listed in equation (35). The same analysis at $x = 0$ just
 797 reverses the sign of the first and third terms.

798 With the $r^{-1/2}$ terms summing to zero (C10) becomes

$$799 \quad \tau = -\Delta\bar{\tau} \left[\frac{\bar{r}^{1/2}}{\sqrt{2+\bar{r}}} - 1 \right] + \nabla\tau w \left[-\frac{2\bar{r}^{1/2} + \bar{r}^{3/2}}{\sqrt{2+\bar{r}}} + 1 + \bar{r} \right] . \quad (\text{C12})$$

800 Taking the derivative yields, in the limit $\bar{r} \rightarrow 0^+$,

$$801 \quad \frac{d\tau}{dr} = -\frac{\Delta\bar{\tau}}{2\sqrt{2}w^{1/2}} r^{-1/2} - \frac{\nabla\tau w^{1/2}}{\sqrt{2}} r^{-1/2} + \nabla\tau . \quad (\text{C13})$$

802 We would like $d\tau/dr$ for $r > 0$ to be continuous with the value $\nabla\tau$ specified as the
 803 boundary condition for $r < 0$. This requires that the $r^{-1/2}$ terms sum to zero, leading to

$$804 \quad -\Delta\bar{\tau} = 2w\nabla\tau . \quad (\text{C14})$$

805 With these constraints we can solve for D , w , $\Delta\bar{\tau}$, and $\nabla\tau$ as described in the main
 806 text. Substituting the results (equations 37–39) back into equations (C2), (C5), and
 807 (C8) and non-dimensionalizing, we obtain the analytical expressions for f and f' used to
 808 approximate the slip and velocity distributions:

$$809 \quad f = \frac{9}{8\pi} \left(1 - \frac{a}{b}\right)^{-1} \left[\frac{\pi}{2} + \sin^{-1} \bar{X} + \frac{4}{3} \sqrt{1 - \bar{X}^2} - \frac{1}{3} \bar{X} \sqrt{1 - \bar{X}^2} \right] , \quad (\text{C15})$$

$$f' = \frac{2}{3} \left(1 - \frac{a}{b}\right) \frac{1 - 2\bar{X} + \bar{X}^2}{\sqrt{1 - \bar{X}^2}}, \quad (\text{C16})$$

where $\bar{X} \equiv (X - W)/W$. Note that with $f'(2W) = 0$ this solution still violates the boundary condition at $X = 2W$ stipulated by equation (21).

Appendix D: Behavior of $V\theta/D_c$ near the stress minimum

We are interested in understanding why $V\theta/D_c$ has a minimum near steady-state behind the pulse tip. First note that equation (A11) for $\ln(V\theta/D_c)$ makes no assumption about self-similarity. Because the last term on the right is zero and $\ln(V_{max}/V_{bg})$ is spatially uniform, to the extent that $\ln(V/V_{max})$ varies little relative to $\Delta\tau/b\sigma$ we expect that $\ln(V\theta/D_c)$ is just offset from $\Delta\tau/b\sigma$ by a constant. Furthermore, with the self-similarity constraint the $\Delta\tau/b\sigma$ and $(1 - a/b)\ln(V_{max}/V_{bg})$ terms become the $g + (1 - a/b)$ that multiplies Ψ_0 in (A12). To the extent that (A12) is dominated by the Ψ_0 -dependent term, $\ln(V\theta/D_c)$ could both have a minimum near the stress minimum and be near steady-state at that point ($g_{min} \sim -[1 - a/b]$, so at $X = X_{gmin}$, $\ln[V\theta/D_c] \sim 0$) (Figure D1a).

Estimating the extent to which the minima in $\ln(V\theta/D_c)$ and $\Delta\tau$ might differ requires evaluating the other terms in (A12). Taking the spatial derivative and writing Ψ for $\ln V\theta/D_c$ leads to

$$\frac{d\Psi}{d\bar{X}} = g'\Psi_0 + \left(1 - \frac{a}{b}\right) \left[\frac{f''}{f'} + \frac{C}{V/(f'V_{max})} \right]. \quad (\text{D1})$$

Closer to the tip than the stress minimum g' is large and negative, with a maximum magnitude of order unity (Figure D1b). In the vicinity of X_{gmin} , the f''/f' term, which accounts for the translation rather than the sharpening of the pulse front, dominates the bracketed expression because the denominator of the second term is of order 1 (Figure 3;

830 the same figure applies nearly unchanged to other a/b after scaling the horizontal axis by
 831 $[1 - a/b]^{-2}$. At X_{gmin} , $g' = 0$ and $f'' < 0$, so $d\Psi/dX < 0$ ($f'' < 0$ because the inflection
 832 point where $f'' = 0$ occurs very close to X_{Vm} , well inboard of X_{gmin}). Thus the minimum
 833 in Ψ , if it exists, occurs outboard of the minimum in $\Delta\tau$.

834 Outside the slip-weakening region, g' is positive and close to $(1 - a/b)^3$ (equation 39).
 835 For a crude estimate of f''/f' we can assume that outboard of X_{gmin} the slip satisfies
 836 the near-tip approximation, $\delta = (2\sqrt{1}/\sqrt{\pi}\mu')K_c\sqrt{x'}$, with K_c given by (7). This leads to
 837 $f(X) \approx (4/\sqrt{\pi})X^{-1/2}$, or

$$838 \quad \frac{f''}{f'} \approx -\frac{1}{2X} . \tag{D2}$$

839 At $X = X_{gmin} \sim 7$, (D2) implies $f''/f' \sim -0.07$; numerically we find the value to be
 840 ~ -0.1 (Figure D1b). For $a/b = 0.9$ and $\Psi_0 > 10$ (that is, $V_{max}/V_{bg} > 10^4$), $(1 - a/b)^2\Psi_0 >$
 841 0.1 , so from (D1) we expect $d\Psi/dX$ to change from negative to positive before g' reaches
 842 the estimate of $(1 - a/b)^3$ from (39). From Figure D1a this occurs by $X = 9$; the actual
 843 minimum of Ψ occurs even closer to X_{gmin} .

844 Qualitatively, we can say that $d\Delta\tau/dX$ passes from negative to positive because of the
 845 transition from the slip-weakening region to the dislocation-like stress field. Then dividing
 846 (D1) by $(1 - a/b)$ and with $g' = (1 - a/b)^3$, $d\Psi/dX$ will pass from negative to positive
 847 at near the same spot unless f''/f' is more negative than $(1 - a/b)^2\Psi_0$ is positive. If
 848 we assume $f = aX^n$, then $f''/f' = (n - 1)X^{-1}$. For a concave, crack-like slip profile,
 849 $0 < n < 1$. Within these bounds f''/f' can be at most twice that in (D2).

850 **Acknowledgments.**

851 This research was supported by NSF grant EAR-0538156. We thank an anonymous
 852 reviewer for detailed comments that helped clarify many aspects of the manuscript.

References

- 853 Ampuero, J.-P., and A. M. Rubin (2008), Earthquake nucleation on rate and state faults
854 – aging and slip laws, *J. Geophys. Res.*, *113*, B01302, doi:10.1029/2007JB005082.
- 855 Bayart, E., A. M. Rubin, and C. Marone (2006), Evolution of fault friction following large
856 velocity jumps, *Eos Trans, AGU*, *87*(52), Fall Meet. Suppl., Abstract S31A-0180.
- 857 Beeler, N. M., T. E. Tullis, and J. D. Weeks (1994), The roles of time and displacement
858 in the evolution effect in rock friction, *Geophys. Res. Lett.*, *21*, 1987–1990.
- 859 Blanpied, M. L., C. J. Marone, D. A. Lockner, J. D. Byerlee, and D. P. King (1998),
860 Quantitative measure of the variation in fault rheology due to fluid-rock interactions,
861 *J. Geophys. Res.*, *103*, 9691–9712.
- 862 Broberg, K. B. (1999), *Cracks and Fracture*, Academic Press, San Diego.
- 863 Chen, T., and N. Lapusta (2009), Scaling of small repeating earthquakes explained by
864 interaction of seismic and aseismic slip in a rate and state fault model, *J. Geophys.*
865 *Res.*, *113*, B01311, doi:10.1029/2008JB005749.
- 866 Dieterich, J. H. (1979), Modeling of rock friction 1. experimental results and constitutive
867 equations, *J. Geophys. Res.*, *84*, 2161–2168.
- 868 Dieterich, J. H. (1992), Earthquake nucleation on faults with rate- and state-dependent
869 friction, *Tectonophys.*, *211*, 115–134.
- 870 Dieterich, J. H. (1994), A constitutive law for rate of earthquake production and and its
871 application to earthquake clustering, *J. Geophys. Res.*, *99*, 2601–2618.
- 872 Dieterich, J. H., and B. D. Kilgore (1994), Direct observation of frictional contacts: New
873 insights for state-dependent properties, *Pageoph.*, *143*, 283–302.

- 874 Dieterich, J. H., and B. D. Kilgore (1996), Implications of fault constitutive properties for
875 earthquake prediction, *Proc. Natl. Acad. Sci. USA*, *93*, 3787–3794.
- 876 Ellsworth, E. L., and G. C. Beroza (1995), Seismic evidence for an earthquake nucleation
877 phase, *Science*, *268*, 851–855.
- 878 Ellsworth, E. L., P. Malin, K. Imanishi, S. Roecker, R. Nadeau, V. Oye, C. Thurber,
879 F. Waldhauser, N. Boness, S. Hickman, and M. Zoback (2007), Seismology inside
880 the fault zone: Applications to fault-zone properties and rupture dynamics, *Scien-
881 tific Drilling, Special Issue No. 1, Part 4: The Physics of Earthquake Rupture*, 84–87,
882 doi:10.2204/iodp.sd.s01.04.2007.
- 883 Kaneko, Y., and N. Lapusta (2008), Variability of earthquake nucleation in continuum
884 models of rate-and-state faults and implications for aftershock rates, *J. Geophys. Res.*,
885 *113*, B12312, doi:10.1029/2007JB005154.
- 886 Kato, N. (2003), A possible model for large preseismic slip on a deeper extension of a
887 seismic rupture plane, *Earth Planet. Sci. Lett.*, *216*, 17–25.
- 888 Kilgore, B. D., M. L. Blanpied, and J. H. Dieterich (1993), Velocity dependent friction of
889 granite over a wide range of conditions, *Geophys. Res. Lett.*, *20*, 903–906.
- 890 Lawn, B. (1993), *Fracture of Brittle Solids - 2nd edition*, Cambridge University Press,
891 Cambridge.
- 892 Liu, Y., and J. R. Rice (2005), Aseismic slip transients emerge spontaneously in three-
893 dimensional rate and state modeling of subduction earthquake sequences, *J. Geophys.
894 Res.*, *110*, B08307, doi:10.1029/2004JB003424.
- 895 Marone, C. (1998), Laboratory-derived friction laws and their application to seismic fault-
896 ing, *Ann. Rev. Earth Planet. Sci.*, *26*, 643–646.

- 897 Nakatani, M. (2001), Conceptual and physical clarification of rate and state friction:
898 Frictional sliding as a thermally activated rheology, *J. Geophys. Res.*, *106*, 13,347–
899 13,380.
- 900 Nakatani, M., and C. H. Scholz (2006), Intrinsic and apparent short-time limits for fault
901 healing: Theory, observations, and implications for velocity-dependent friction, *J. Geo-
902 phys. Res.*, *111*, B12208, doi:10.1029/2005JB004096.
- 903 Olson, E. L., and R. M. Allen (2005), The deterministic nature of earthquake rupture,
904 *Nature*, *438*, 212–215, doi:10.1038/nature04214.
- 905 Perrin, G., J. R. Rice, and G. Zheng (1995), Self-healing slip pulse on a frictional surface,
906 *J. Mech. Phys. Solids*, *43*, 1461–1495.
- 907 Reches, Z., M. Johnston, T. Jordan, T. Onstott, and M. Zoback (2004), Natural earth-
908 quake laboratory in South African mines: Drilling active faults and monitoring their
909 seismicity, *Geophys. Res. Abstracts*, *6*(06305), European Geosciences Union.
- 910 Rice, J. R. (1993), Spatio-temporal complexity of slip on a fault, *J. Geophys. Res.*, *98*,
911 9885–9907.
- 912 Rice, J. R., N. Lapusta, and K. Ranjith (2001), Rate- and state-dependent friction friction
913 and the stability of sliding between elastically deformable solids, *J. Mech. Phys. Sol.*,
914 *49*, 1865–1898.
- 915 Rubin, A. M. (2008), Episodic slow slip events and rate-and-state friction, *J. Geophys.*
916 *Res.*, *113*, B11414, doi:10.1029/2008JB005642.
- 917 Rubin, A. M., and J.-P. Ampuero (2005), Earthquake nucleation on (aging) rate and state
918 faults, *J. Geophys. Res.*, *110*, B11312, doi:10.1029/2005JB003686.

- 919 Ruina, A. (1983), Slip instability and state variable friction laws, *J. Geophys. Res.*, *88*,
920 10,359–10,10,370.
- 921 Secor, D., and D. Pollard (1975), On the stability of open hydraulic fractures in the earth's
922 crust, *Geophys. Res. Lett.*, *2*, 510–513.
- 923 Segall, P., and J. R. Rice (2006), Does shear heating of pore fluid contribute to earthquake
924 nucleation?, *J. Geophys. Res.*, *111*, B11312, doi:10.1029/2005JB004129.
- 925 Shibazaki, B., and Y. Iio (2003), On the physical mechanism of silent slip events
926 along the deeper part of the seismogenic zone, *Geophys. Res. Lett.*, *30*, 1489, doi:
927 10.1029/2003GL017047.

Table 1. Notation

Parameter	Description
$a; b$	Coefficients of the rate-and-state direct and evolution effects (eq. 1)
C	Acceleration coefficient (eqs. 19 and B4)
C_{age}	Acceleration coefficient in the crack-expansion regime of aging-law nucleation (eq. 27)
D	Total slip within pulse (analytical approximation)
D_c	Characteristic slip distance in the evolution law
f, f'	Slip function and its spatial derivative (eq. 17)
g, g'	Stress drop function and its derivative (eq. 20)
g_{min}	g at the stress minimum behind the pulse front
G	Mechanical energy release rate (eq. 9)
G_c	Fracture energy (eq. 5)
K_c	Fracture toughness (eq. 7)
l	Location of pulse front
L	Characteristic nucleation length scale
L_b	Relevant length scale for $V\theta/D_c \gg 1$ (eq. 8)
p	Slip growth exponent (eq. 11)
R	Length of the slip-weakening region behind the pulse front (eq. 16)
t^*	Time of instability
V	Slip speed
V_{bg}	Background slip speed prior to the approach of the pulse front
V_{max}	Maximum slip speed behind the pulse front
V_{prop}	Propagation speed of the pulse front
w	Pulse half-width
W	Scaled normalized pulse half-width $(w/L_b)\Psi_0$ (eq. 40)
x'	Distance behind the pulse front
X	Scaled normalized distance behind the pulse front $(x'/L_b)\Psi_0$ (eq. 17)
$X_{V_m}; f'_{V_m}$	X and f' evaluated at the location of V_{max}
δ	Slip distance
δ_c	Effective slip-weakening distance at the pulse front
θ	State variable
θ_{bg}	Value of θ prior to the arrival of the pulse front
μ'	μ (anti-plane strain) or $\mu/(1 - \nu)$ (plane strain), where μ is shear modulus and ν is Poisson's ratio
σ	Effective normal stress
τ	Shear stress
$\Delta\tau$	Stress drop
$\Delta\tau_{min}$	$\Delta\tau$ at the stress minimum behind the pulse front
$\Delta\tau_{p-r}$	Peak-to-minimum strength drop at the pulse front
$\Delta\bar{\tau}$	Average stress drop within the pulse (analytical approximation)
$\nabla\tau$	Stress gradient within the pulse (analytical approximation)
Ψ_{bg}	$\ln(V_{max}\theta_{bg}/D_c)$; determines the fracture energy

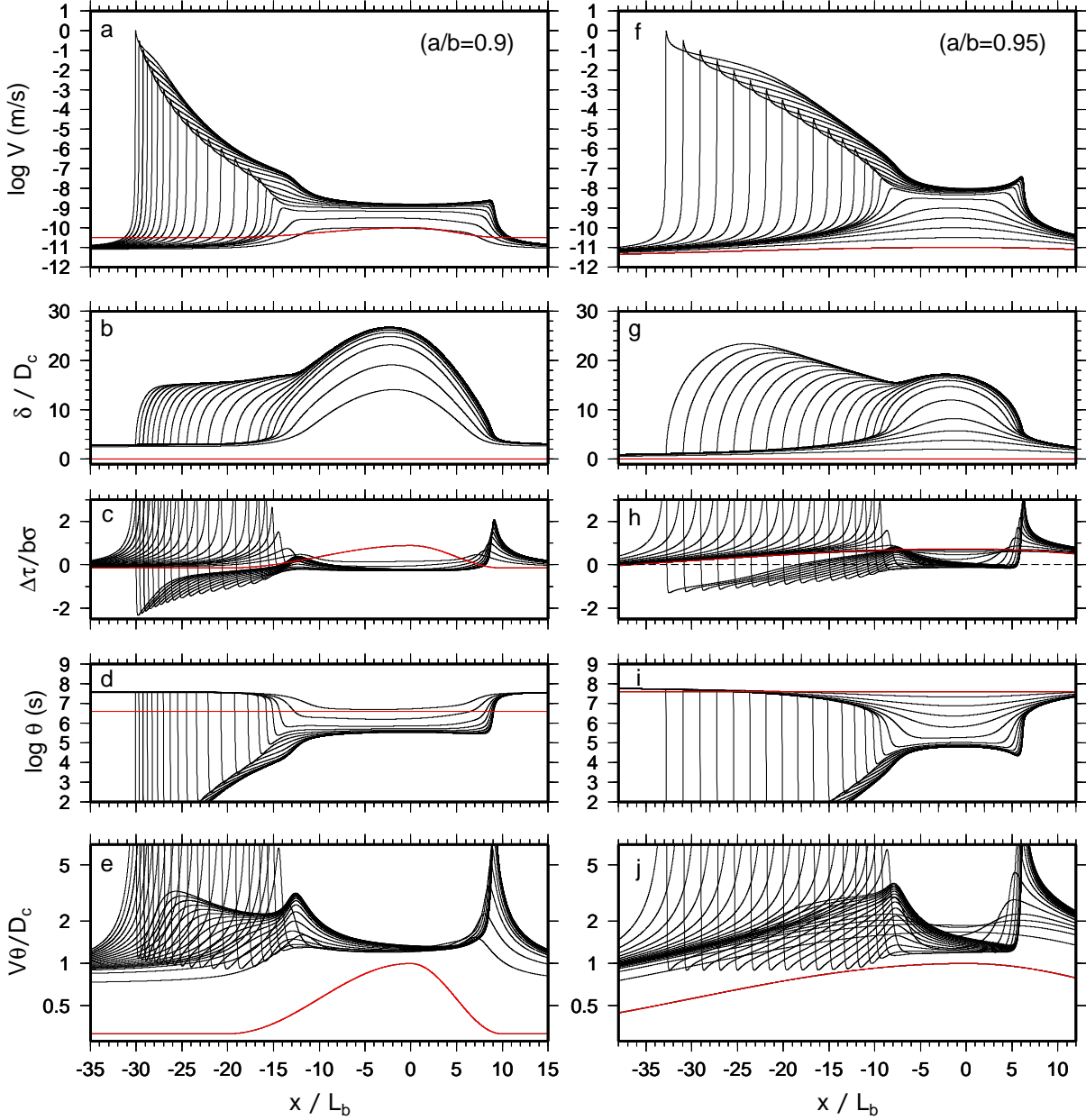


Figure 1. Snapshots of (top row) slip speed, (second row) normalized slip, (third row) normalized stress drop, (fourth row) state, and (bottom row) proximity to steady state, as a function of normalized position, for 2 styles of slip pulses observed by *Ampuero and Rubin* [2008]. Initial conditions are shown by the red curves and values of a/b are specified in the top panels. The simulations are stopped when V_{max} reaches 1 m/s, somewhat beyond the limit of applicability of the quasi-static equations used.

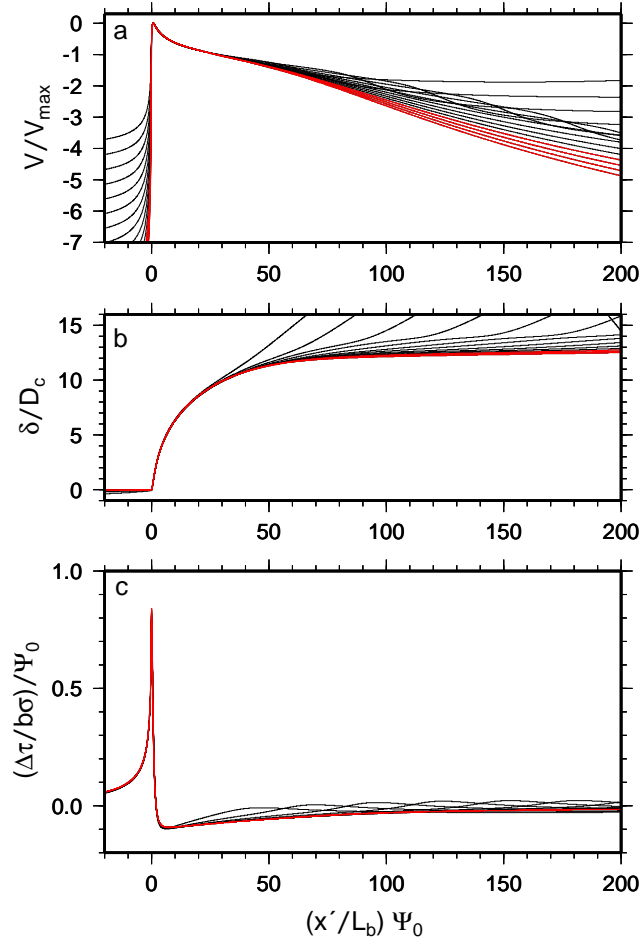


Figure 2. Snapshots of (a) slip speed normalized by the current maximum, (b) normalized slip, and (c) scaled normalized stress drop, as a function of scaled normalized distance behind the pulse tip, showing the approach to self-similarity for the slip pulse in the left column of Figure 1. The pulse tip is defined as the location of peak stress; slips in (b) are relative to the slip at that point. All snapshots with maximum slip speeds $\geq 10^{-7}$ m/s are shown; red curves show the last 4 snapshots. At the time of the last snapshot $\Psi_0 = 25.3$, so a value of 50 on the horizontal axis in Figure 2 corresponds to a distance of roughly $2L_b$ behind the last pulse tip shown in Figure 1.

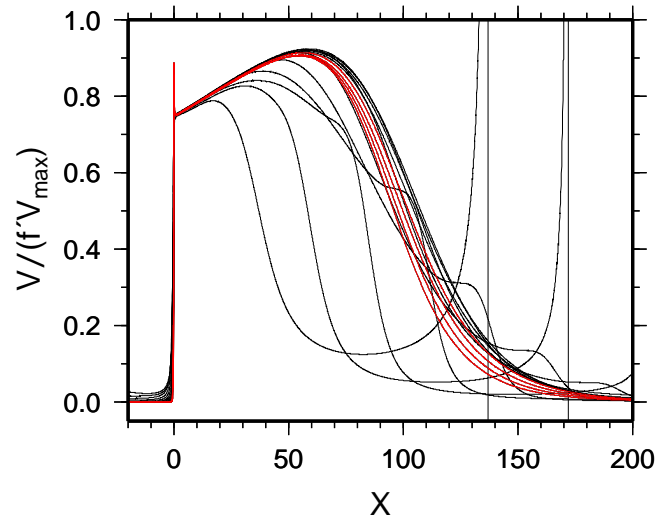


Figure 3. Snapshots of $V/f'V_{max}$ for the snapshots of Figure 2, as a function of $X = (x'/L_b)\Psi_0$. If V/V_{max} a function of X only, equation (18) implies collapse to a line of slope C . The “spike” at $X = 0$ comes from the error in determining the slip gradient f' via centered finite differences at the grid point closest to the pulse tip.

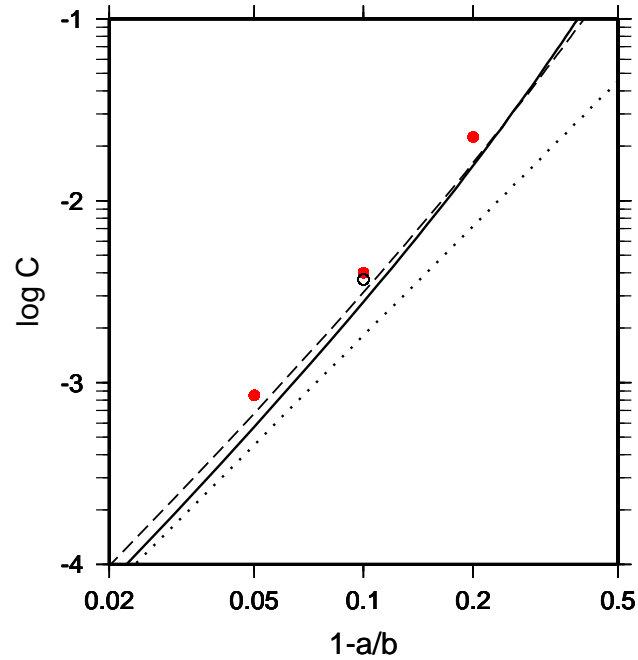


Figure 4. Solid curve, estimate of the acceleration constant C as a function of $(1 - a/b)$ determined by evaluating equation (42) at $X = W$; dashed curve, the same but with (42) evaluated at $X = 0.5W$. Dotted line shows the asymptotic result for $a/b \sim 1$ corresponding to the solid curve. Red dots show the numerical values derived from evaluating the right side of equation (19) at $V_{max} = 1$ m/s for the examples in Figure 5, and black circle the numerical value via the same method but for the example in Figure 2.

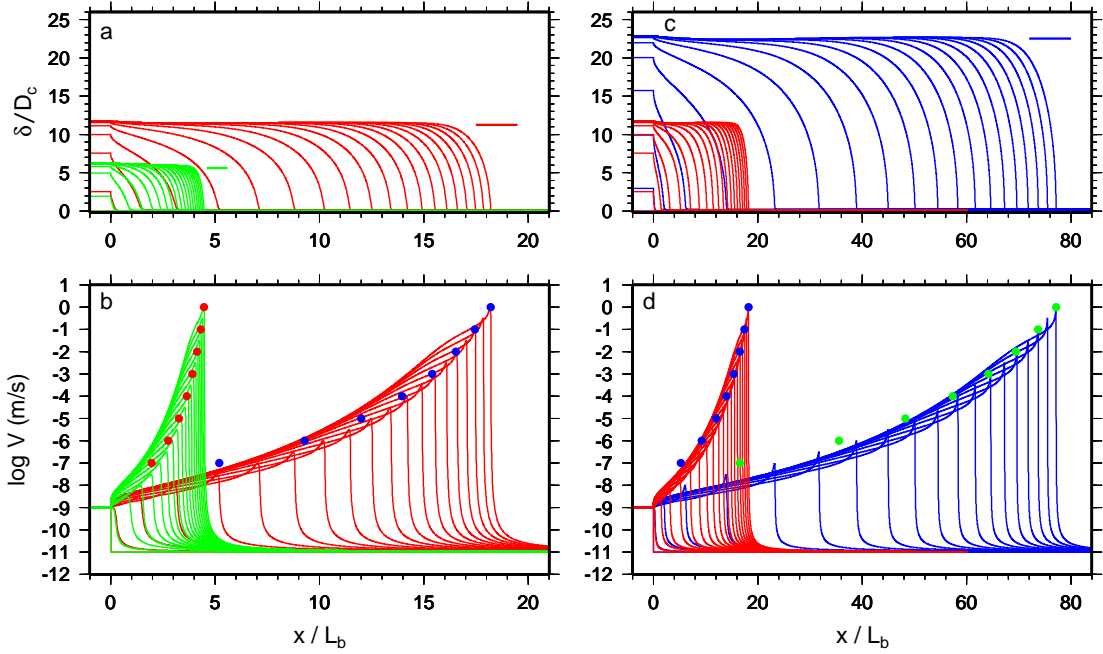


Figure 5. Examples of slip pulses where the fault was forced to slide at $V = 10^{-9}$ m/s for $x < 0$, and was initially sliding at steady state with $V = 10^{-11}$ m/s for $x \geq 0$. Green curves, $a/b = 0.8$; red, $a/b = 0.9$; blue, $a/b = 0.95$. The horizontal lines in the top row show the expected slip from (38). The colored dots in the bottom row show the expected locations of the pulse front from (33), relative to the final snapshot, with C extracted from Figure 6 at $V_{max} = 1$ m/s.

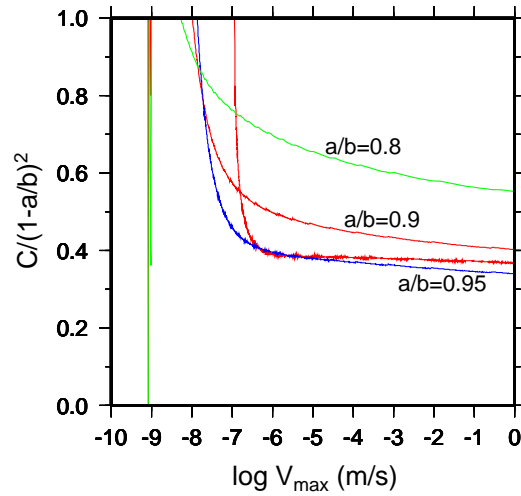


Figure 6. Plots of C as a function of V_{max} from the simulations in Figure 5, normalized by $(1 - a/b)^2$, determined from equation (19) by differentiating the numerical output to obtain \dot{V}_{max} . Red curve that is nearly constant for $V_{max} \gtrsim 10^{-6}$ m/s is from the simulation in Figure 1a ($a/b = 0.9$).

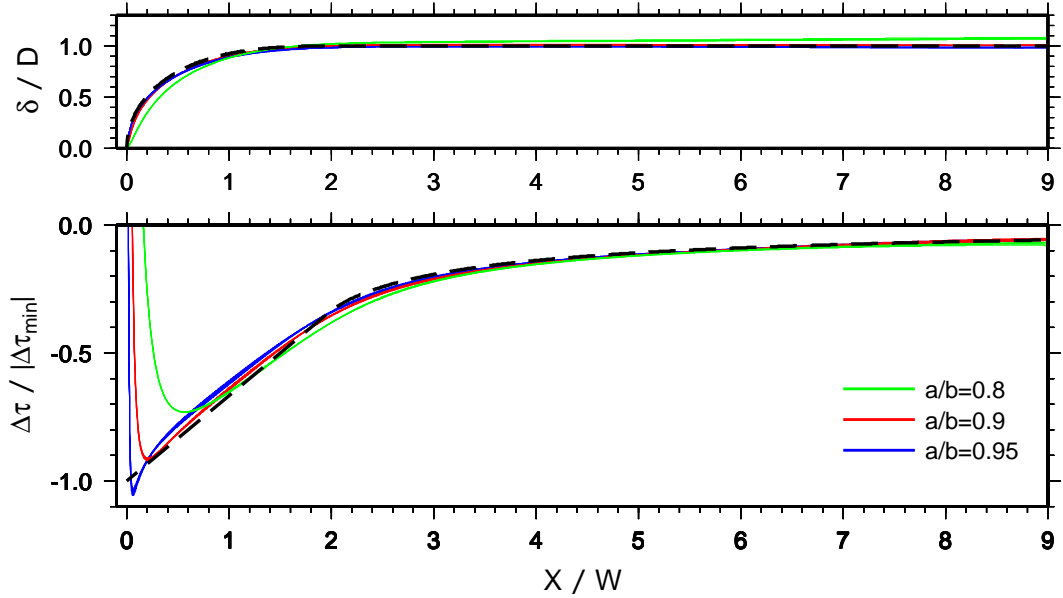


Figure 7. Comparison of the analytical finite pulse approximation (dashed line) to the last 5 snapshots from the numerical simulations in Figure 5. Pulse width is $2W$. (a), Slip normalized by D from (38); (b), stress drop normalized by $\Delta\tau_{min}$ from (37).

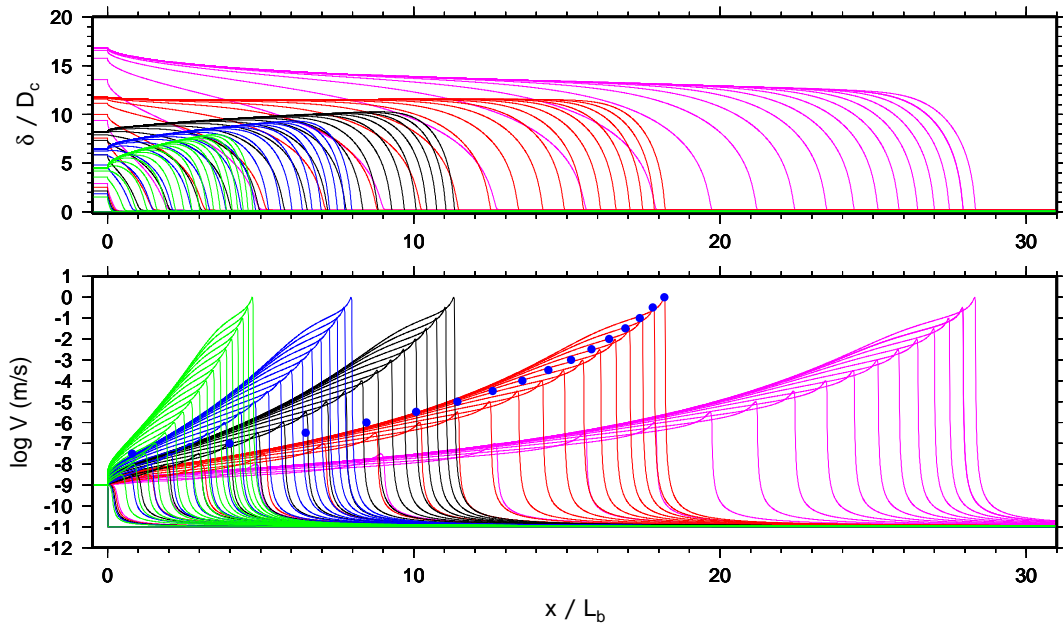


Figure 8. Examples of slip pulses with $a/b = 0.9$ where the fault was forced to slide at $V = 10^{-9}$ m/s for $x < 0$ and where initially $V = 10^{-11}$ m/s for $x \geq 0$. From left (green curves) to right the initial values of $V_{bg}\theta_{bg}/D_c$ were 4 (above steady state), 2, 1.4, 1, and 0.8 (below steady state). Top, normalized slip; bottom, log slip speed.

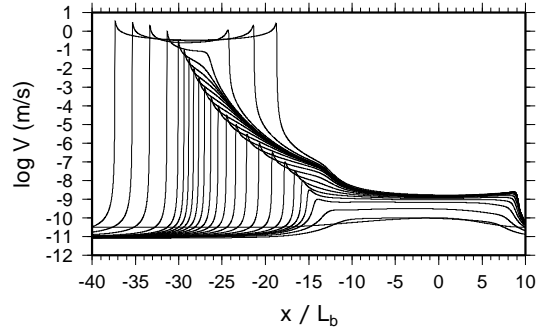


Figure 9. Snapshots from a simulation identical to than in Figure 1a except for the addition of radiation damping, meaning that the term $V\mu/2c_s$ has been added to the right side of equation (1), where μ is the shear modulus and c_s the shear wave speed [Rice, 1993]. Radiation damping is expected to become important when the slip speed exceeds a value $V_{dym} \sim 2a\sigma\beta/\mu$ [Rubin and Ampuero, 2005], which is roughly 0.6 m/s in this example. Snapshots are plotted at every half-magnitude increase in V_{max} until 1 m/s, and then every $2L_b$ of propagation of the left front. When acceleration of slip is slowed by dynamics, the quasi-static slip pulse gives rise to a bilateral rupture. The propagation speed of the right rupture front is larger than that of the left, even though its peak slip speed is slightly less, because the quasi-static phase of nucleation has made θ_{bg} to the right smaller (equation 31).

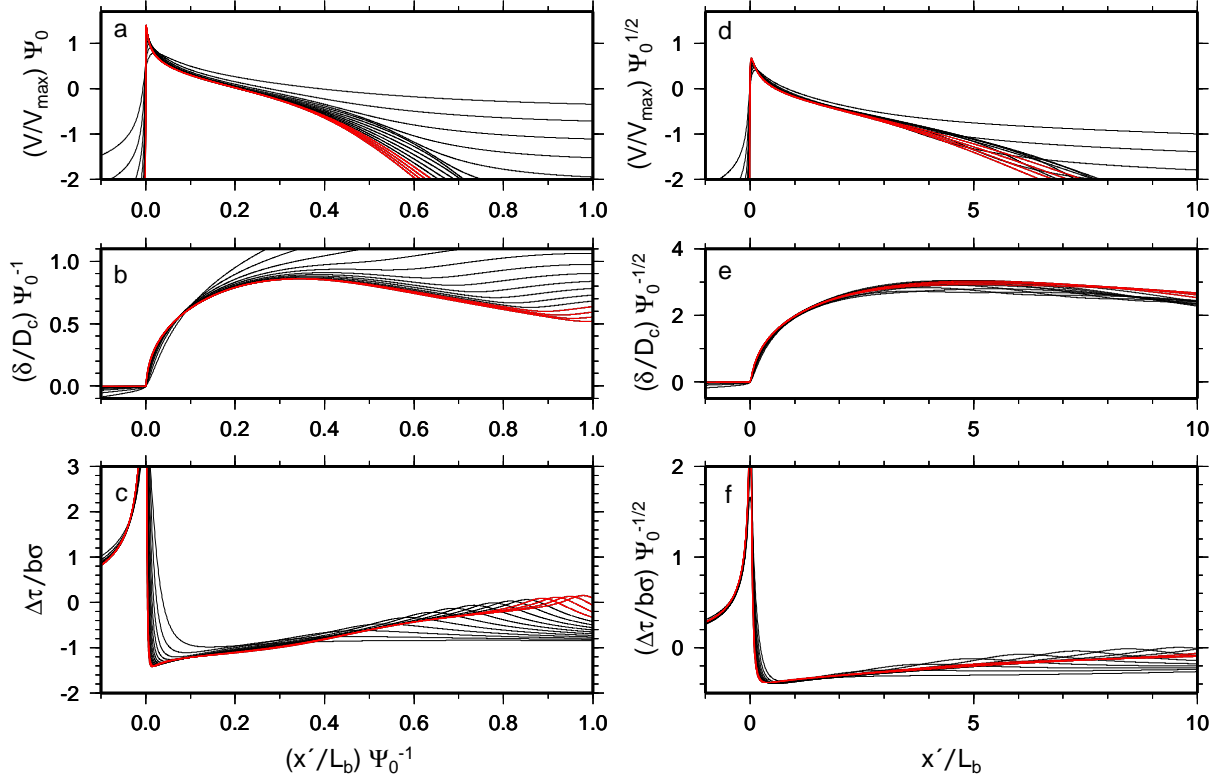


Figure B1. Snapshots of (top row) normalized slip speed, (middle row) normalized slip, and (bottom row) normalized stress drop, all scaled by the appropriate power of Ψ_0 , as a function of scaled normalized position, for (left column) $p = 1$ (right column of Figure 1) and (right column) $p = 1/2$ (right column of Figure 7 of *Ampuero and Rubin [2008]*). In both cases $a/b = 0.95$. Snapshots with V_{max} from 10^{-7} to 1 m/s are shown ($\Psi_0 = 6.2$ – 25.6 , left, and 6.6 – 22.7 , right); last 4 are in red. Scaling is consistent with equations (B1), (B2), and (B7).

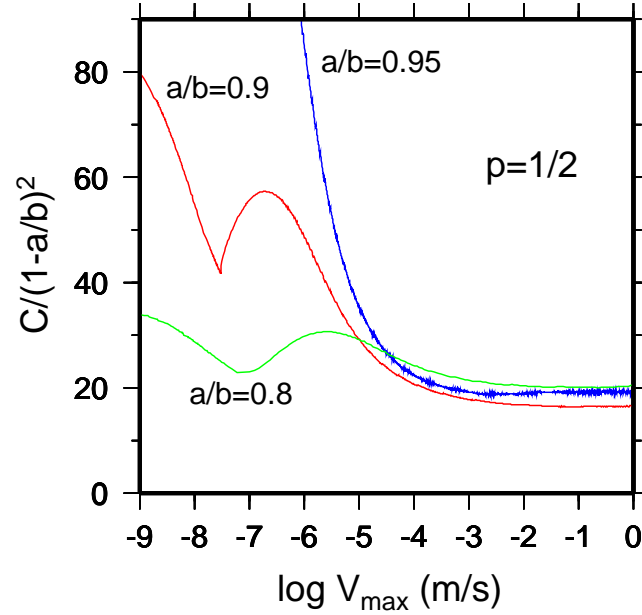


Figure B2. Plots of C as a function of V_{max} , determined by evaluating equation (B4) numerically, for 3 simulations with $p = 1/2$ and $a/b = 0.8, 0.9,$ and 0.95 (those in Figure 7 of *Ampuero and Rubin* [2008]). As for the case $p = 0$, C is approximately proportional to $(1 - a/b)^2$, but the definition of C and the coefficient of proportionality differ.

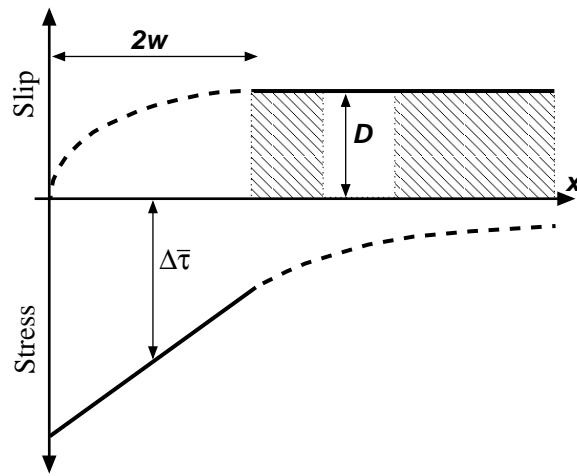


Figure C1. Schematic diagram for the superposition problem. Unknowns to be determined are the pulse width $2w$, the total slip D , and the average stress drop $\Delta\bar{\tau}$ and stress gradient $\nabla\tau$ within the pulse. The slip over $0 < x < 2w$ and stress for $x > 2w$ are then determined from elasticity.

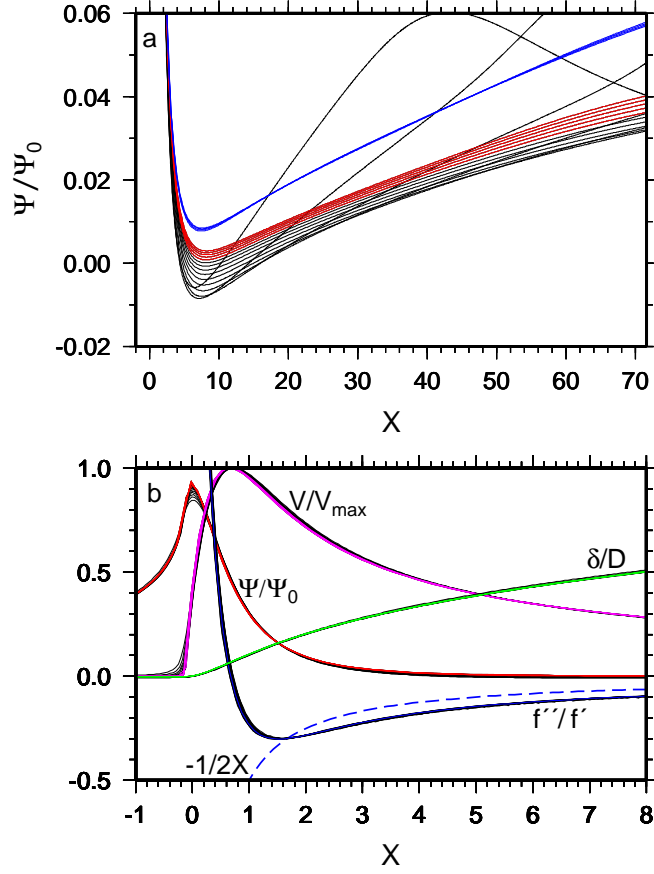


Figure D1. (a) Snapshots of $\ln(V\theta/D_c)/\Psi_0$ as a function of $X = (x'/L_b)\Psi_0$, over the pulse width $X \leq 2W$, for the case $p = 0$, $a/b = 0.9$ in Figures 1 and 2. Snapshots from $V_{max} = 10^{-7}$ to 1 m/s ($\Psi_0 = 8.8$ – 25.3) are shown, with the last 5 in red. For comparison, the blue curves show the last 5 snapshots of $g + (1 - a/b)$, whose minimum as explained in Section 6 differs from zero by roughly $(1 - a/b)^2$. For this and all other values of a/b and p , $V\theta/D_c$ has a minimum near steady-state close to the minimum in $\Delta\tau$. (b) Snapshots, from $V_{max} = 10^{-7}$ to 1 m/s, of V/V_{max} , δ/D , Ψ/Ψ_0 , f''/f' , and for comparison $-1/2X$ (equation D2), as a function of X , in a zoom close to the pulse front.